Article

SOURCE DATA | TRANSPARENT PROCESS | OPEN ACCESS

THE EMBO JOURNAL

Fxr1 regulates sleep and synaptic homeostasis

Jivan Khlghatyan[1,2,†], Alesya Evstratova[1], Lusine Bozoyan[1], Simon Chamberland[2,‡], Dipashree Chatterjee[1], Aleksandra Marakhovskaia[1], Tiago Soares Silva[1], Katalin Toth[3], Valerie Mongrain[4] & Jean-Martin Beaulieu[1,*]

Abstract

The fragile X autosomal homolog 1 (Fxr1) is regulated by lithium and has been GWAS-associated with schizophrenia and insomnia. Homeostatic regulation of synaptic strength is essential for the maintenance of brain functions and involves both cell-autonomous and system-level processes such as sleep. We examined the contribution of Fxr1 to cell-autonomous homeostatic synaptic scaling and neuronal responses to sleep loss, using a combination of gene overexpression and Crispr/Cas9-mediated somatic knockouts to modulate gene expression. Our findings indicate that Fxr1 is downregulated during both scaling and sleep deprivation via a glycogen synthase kinase 3 beta (GSK3β)-dependent mechanism. In both conditions, downregulation of Fxr1 is essential for the homeostatic modulation of surface AMPA receptors and synaptic strength. Preventing the downregulation of Fxr1 during sleep deprivation results in altered EEG signatures. Furthermore, sequencing of neuronal translatomes revealed the contribution of Fxr1 to changes induced by sleep deprivation. These findings uncover a role of Fxr1 as a shared signaling hub between cell-autonomous homeostatic plasticity and system-level responses to sleep loss, with potential implications for neuropsychiatric illnesses and treatments.

Keywords allostatic load; Fxr1; scaling; sleep deprivation; synaptic homeostasis
Subject Category Neuroscience
DOI 10.15252/embj.2019103864 | Received 29 October 2019 | Revised 1 August 2020 | Accepted 6 August 2020 | Published online 7 September 2020
The EMBO Journal (2020) 39: e103864

Introduction

Regulation of synaptic strength is essential for the maintenance of proper brain functions, and its disruption contributes in circuit-level imbalance of excitatory and inhibitory activity in neuropsychiatric illnesses such as Alzheimer disease, autism, and schizophrenia (Gao & Penzes, 2015; Nelson & Valakh, 2015; Vico Varela *et al*, 2019). Homeostatic mechanisms, engaged in response to external conditions, are believed to contribute to this regulation both at a cell autonomous and system level (Vyazovskiy *et al*, 2008; Turrigiano, 2012; Vitureira *et al*, 2012; Tononi & Cirelli, 2014; Hengen *et al*, 2016; Diering *et al*, 2017). However, the relationship between these different spatial scales of regulation is unclear.

Synaptic scaling is a form of cell-autonomous homeostatic plasticity used by neurons to maintain net firing rates and is achieved by the modulation of postsynaptic AMPA receptors (Turrigiano, 2008). Prolonged inhibition of neuronal activity induces a multiplicative increase in miniature excitatory postsynaptic currents (mEPSCs) (upscaling) via increase in postsynaptic AMPA receptors. The opposite (downscaling) occurs as a result of prolonged neuronal activation (Turrigiano *et al*, 1998). However, it should be noted that in addition to global scaling, which affects the whole cell, forms of synapse selective homeostatic scaling have also been reported (Beique *et al*, 2011).

At the system level, homeostatic regulatory mechanisms are engaged during the sleep/wake cycle. Homeostatic sleep pressure accumulates during wake and dissipates during sleep (Mang & Franken, 2015). Moreover, neuronal activity correlates with sleep pressure by increasing during wake and decreasing during sleep (Vyazovskiy *et al*, 2008; Liu *et al*, 2010; Tononi & Cirelli, 2014) and neuronal activity increases following prolonged wakefulness a change that can be reversed by a recovery sleep period (Vyazovskiy *et al*, 2008; Liu *et al*, 2010; Tononi & Cirelli, 2014).

Some lines of evidence suggest that molecular and structural changes involved in scaling also occur during sleep (Diering *et al*, 2017; de Vivo *et al*, 2017). This raises the question of whether there are common homeostatic molecular regulators of neuronal activity involved in cell-autonomous synaptic scaling and system-level sleep regulation.

The fragile X mental retardation autosomal homolog 1 (Fxr1) might play a role both in sleep and in homeostatic AMPA receptor regulation. Fxr1 is an RNA-binding protein that is expressed in different types of brain cells. In neurons, Fxr1 is localized in the cell bodies and dendrites in association with mRNAs and ribosomes

1 Department of Pharmacology & Toxicology, University of Toronto, Toronto, ON, Canada
2 Department of Psychiatry and Neuroscience, Faculty of Medicine, Université Laval, Québec-City, QC, Canada
3 Department of Cellular and Molecular Medicine, Faculty of Medicine, University of Ottawa, Ottawa, ON, Canada
4 Department of Neuroscience, Université de Montréal and Center for Advanced Research in Sleep Medicine, Hôpital du Sacré-Coeur de Montréal (CIUSSS-NIM), Montreal, QC, Canada
*Corresponding author. Tel: +1 416 978 1125; E-mail: martin.beaulieu@utoronto.ca
†Present address: Department of Neuroscience, Novartis Institutes for Biomedical Research, Cambridge, MA, USA
‡Present address: NYU Neuroscience Institute, Langone Medical Center, New York University, New York, NY, USA

© 2020 The Authors. Published under the terms of the CC BY NC ND 4.0 license

(Cook *et al*, 2011). Variants of the *FXR1* locus are GWAS-identified risk factors for insomnia (Jansen *et al*, 2019), and a schizophrenia-associated *FXR1* variant is linked to sleep duration (Dashti *et al*, 2019). Interestingly, Fxr1 protein degradation is regulated by glycogen synthase kinase 3 beta (Gsk3β) (Del'Guidice *et al*, 2015; Qie *et al*, 2017) and its brain expression is increased in response to lithium, a pharmacological agent used for the treatment of psychiatric disorders, such as bipolar disorder, and of associated sleep disturbances (Billiard, 1987; Freland & Beaulieu, 2012).

Fxr1, together with Fxr2, is an autosomal paralog of the fragile X mental retardation protein Fmrp, which is needed for the regulation of synaptic scaling by retinoic acid (Soden & Chen, 2010; Lee *et al*, 2018). Fxr2 and Fmrp have been shown to regulate synaptic expression of the AMPA receptor GluA1 subunit in different brain regions (Guo *et al*, 2015; Khlghatyan & Beaulieu, 2018; Khlghatyan *et al*, 2018). Fxr1 has been shown to regulate *de novo* synthesis of the AMPA receptor GluA2 subunit during long-lasting synaptic potentiation of hippocampal neurons (Cook *et al*, 2014). Nevertheless, the roles of Fxr1 in regulating brain functions, and in particular those related to homeostatic mechanisms, mostly remain to be defined.

The association of Fxr1 with insomnia led us to test whether it can be a regulator of homeostatic plasticity and responses to sleep loss. Our results indicate that Fxr1 is downregulated at a post-transcriptional level by synaptic upscaling and sleep loss via a Gsk3β–dependent mechanism leading to its degradation. Furthermore, downregulation of Fxr1 is essential and sufficient for the regulation of synaptic AMPA receptors in both cell-autonomous homeostatic plasticity and the network response to sleep loss, thus reveling a shared molecular underpinning between different scales of homeostatic regulation of synaptic strength.

Results

Fxr1 protein expression is reduced by homeostatic synaptic scaling

We evaluated the impact of homeostatic plasticity on Fxr1 in primary cortical cultures. Upscaling was induced by adding tetrodotoxin (TTX) to the cell culture media to block neuronal firing for a period of 48 h. To cause downscaling, the GABA-A receptor antagonist bicuculline (BIC) was used to increase neuronal excitability for the same time period (Turrigiano *et al*, 1998).

Protein levels of all Fxr1 isoforms decreased during upscaling (TTX vs. vehicle) (Fig 1A), but did not change during downscaling (BIC vs. vehicle) (Fig 1B). In contrast, Fxr2 levels were marginally decreased (Fig 1C), while Fmrp levels were not affected by upscaling (Fig 1D). Upscaling did not affect mRNA levels of Fxr1 and Fxr2 (Fig 1E and F) and increased levels of Fmrp-encoding mRNA (*Fmr1*) (Fig 1G). This indicates that Fxr1 is the fragile X family protein that is the most affected by upscaling and that this regulation occurs at a post-transcriptional level.

We have previously shown that Gsk3β negatively regulates Fxr1 by targeting the protein for degradation (Del'Guidice *et al*, 2015). Accordingly, together with the decrease in Fxr1 protein, upscaling resulted in an increase in Gsk3α and β activity, resulting from a reduction in the inhibitory phosphorylation of Ser-21/9 (Fig 1H–J). Conversely, the inhibition of Gsk3α and Gsk3β by lithium increased Fxr1 protein levels (Fig 1H–J). Overall, this shows that Fxr1 protein is downregulated specifically during upscaling and that this process involves Gsk3 activity.

Fxr1 stimulates GluA1 expression during upscaling

To investigate whether the decrease in Fxr1 protein is contributing to upscaling, we verified whether an augmentation of Fxr1 could block upscaling. AMPA receptor expression is known to be modulated during homeostatic scaling (Diering *et al*, 2014). Thus, we addressed whether Fxr1 can negatively regulate AMPA receptor expression during scaling.

Neuronal cultures were infected with high efficiency by AAV SYN GFP-Fxr1 (Fxr1) or AAV SYN GFP (Ctrl) (Figs 2A, and EV1A and B). While GFP was equally expressed in all parts of neurons, GFP-Fxr1 brightly labeled cell bodies and appeared as granules in dendrites (Fig 2G), as previously reported in cultured hippocampal neurons (Cook *et al*, 2014). Following infection, we performed Western blot measurement of GluA1 and GluA2 protein levels after TTX or BIC treatment to induce either upscaling or downscaling. Total GluA1 protein increased in Ctrl TTX condition as compared to Ctrl Vehicle (Fig 2B). No changes in total GluA1 protein were observed during downscaling (Fig 2C). Total GluA2 protein did not change during upscaling (Fig EV1D) or downscaling (Fig EV1F).

Surprisingly, the increase in GluA1 protein expression was exacerbated following TTX treatment (Fxr1 TTX vs. Ctrl TTX) in neurons overexpressing Fxr1 (Fig 2B). Consistently with the results at the protein level, GluA1 mRNA increased in Ctrl TTX condition compared with Ctrl Veh and this increase was also further exacerbated in Fxr1 TTX condition (Fxr1 TTX vs. Ctrl TTX) (Fig 2D). This indicates that the increase in GluA1 protein during upscaling can result from a positive regulation by Fxr1 at the mRNA level. To investigate whether Fxr1 can directly bind to GluA1 mRNA, we tagged a luciferase cDNA with 5′UTR, different coding (CDS), or 3′UTR sequences from the GluA1 (*Gria1*) mRNA (Fig 2E) and performed dual-luciferase assays. We detected an increase in the luciferase signal for CDS 1–900, CDS 900–1,800, and 3′UTR constructs under Fxr1 overexpression in comparison with control (Fig 2F). This suggests that Fxr1 positively regulates GluA1 level during upscaling via direct binding to its mRNA and facilitating its translation.

Fxr1 suppresses the increase in surface GluA1 during upscaling

Along with expression, surface levels of AMPA receptor are also changed during homeostatic scaling (Diering *et al*, 2014). Thus, we investigated the effect of Fxr1 on surface levels of AMPA receptors during upscaling and downscaling. Surface expression of the GluA2 subunit did not change during upscaling or downscaling (Fig EV1C and E). Surface expression of GluA1 increased during upscaling in Ctrl (Ctrl TTX vs. Ctrl vehicle), and this increase was abolished by Fxr1 overexpression (Fxr1 TTX vs. Fxr1 overexpression vehicle) (Fig 2G and H). The decrease in surface GluA1 during downscaling was similar in both Ctrl and Fxr1 overexpression conditions (Fig 2G and H). No differences in surface GluA1 expression were observed between Ctrl vehicle and Fxr1 overexpression vehicle conditions (Fig 2G and H). This indicates that an increase in Fxr1 can specifically block the increase in surface GluA1 during upscaling.

 © 2020 The Authors

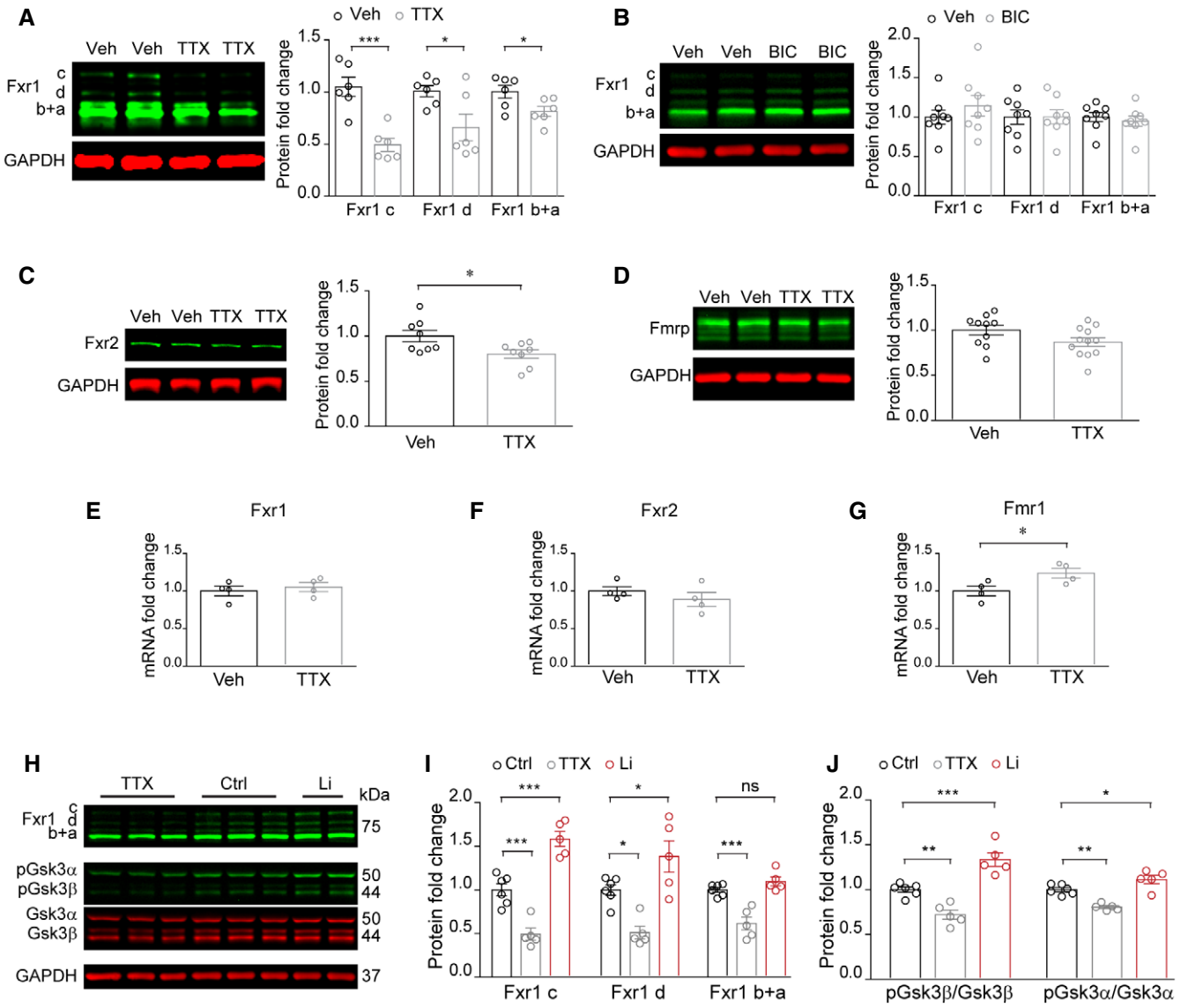

Figure 1. Fxr1 protein expression is decreased during homeostatic synaptic upscaling.

A, B Western blot analysis of Fxr1 during (A), TTX (48 h treatment) induced upscaling (n = 6 in each condition) and (B), BIC (48 h treatment) induced downscaling (n = 8 in each condition) of primary postnatal cortical cultures. Student's t-test $^*P < 0.05$, $^{***}P < 0.001$.

C, D Western blot analysis of (C), Fxr2 (Veh n = 8, TTX n = 8) and (D), Fmrp (Veh n = 10, TTX n = 12) during upscaling, Student's t-test $^*P < 0.05$.

E–G RT–qPCR measurement of mRNA for (E), Fxr1, (F), Fxr2, (G), and Fmr1 during upscaling. n = 4 in each condition, Student's t-test $^*P < 0.05$.

H Western blot analysis for Fxr1, pGsk3α/β, Gsk3α/β, and GAPDH in neuronal cultures treated with 1 μM TTX (TTX) or 1 mM LiCl (Li) or 1 mM NaCl (Ctrl) for 48 h.

I Expression of Fxr1 protein in TTX (n = 5) and Li (n = 5) conditions relative to Ctrl (n = 6) condition. One-way ANOVA with Dunnett's multiple comparison test $^*P < 0.05$, $^{**}P < 0.01$, $^{***}P < 0.001$.

J Expression of pGsk3β/Gsk3β or pGsk3α/Gsk3α in TTX (n = 5) and Li (n = 5) conditions relative to Ctrl (n = 6) condition. One-way ANOVA with Dunnett's multiple comparison test $^*P < 0.05$, $^{**}P < 0.01$, $^{***}P < 0.001$.

Data information: Error bars are ± SEM.
Source data are available online for this figure.

Overall, this shows that the augmentation of Fxr1 blocks the increase in surface GluA1 during upscaling without directly inhibiting GluA1 expression. Furthermore, this suggests that downregulation of Fxr1 can be required for the increase in surface GluA1 during upscaling.

Fxr1 downregulation is necessary and sufficient for the induction of multiplicative upscaling

Upscaling is a cell-autonomous process indexed by a multiplicative increase in miniature excitatory postsynaptic currents (mEPSCs)

© 2020 The Authors

(Turrigiano *et al*, 1998; Turrigiano, 2008). Fxr1 protein expression is downregulated, likely via a lithium-sensitive Gsk3-dependent mechanism, and controls surface GluA1 during upscaling (Figs 1 and 2). Thus, we tested whether the Gsk3β-Fxr1 signaling module regulates synaptic currents during upscaling.

To address the relative contribution of Fxr1 and Gsk3β to upscaling, we used a combination of gene overexpression and Crisps/Cas9-mediated gene inactivation. We designed series of *Fxr1* gene targeting guide RNAs (gRNAs) and verified their efficiency at targeting the mouse genome using Neuro2A cells (Fig EV2A–C). The most efficient *Fxr1* targeting gRNA and a previously characterized *Gsk3β* targeting gRNA (Khlghatyan *et al*, 2018) were used for Crispr/Cas9-mediated gene inactivation in neuronal cultures. All control plasmids contained scrambled gRNAs. An expression vector encoding GFP-Fxr1 and a control vector expressing GFP alone were used for overexpression experiments.

We generated Fxr1 knockout (KO) and Fxr1 Ctrl (both tagged with mCherry), and Gsk3β KO and Gsk3β Ctrl (both tagged with GFP) constructs and performed low-efficiency transfection of neuronal cultures (Fig EV2D). Immunofluorescent staining revealed

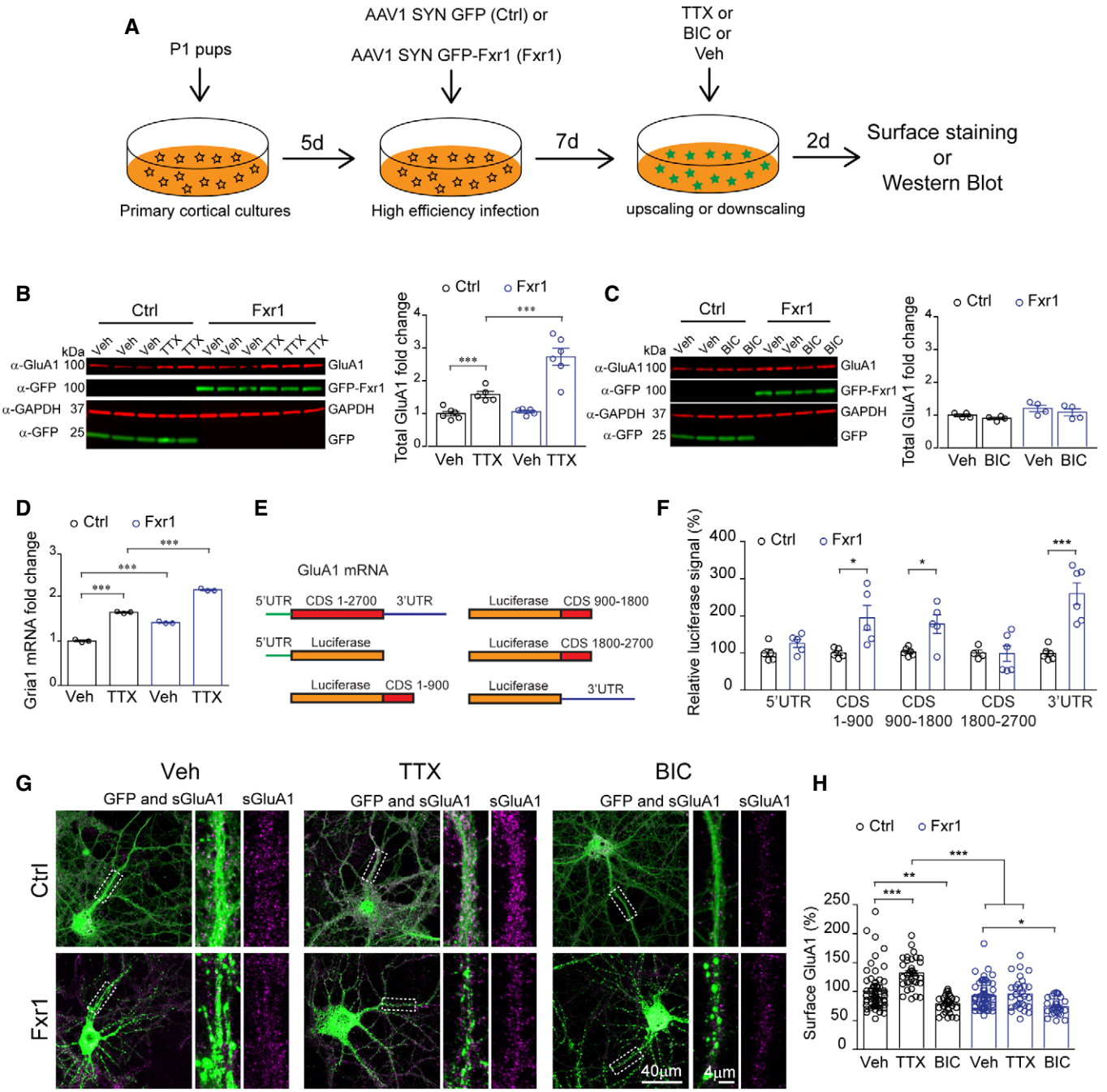

Figure 2.

© 2020 The Authors

Figure 2. Fxr1 suppresses the increase in surface GluA1 during synaptic upscaling.

A Schematic of high-efficiency infection of neuronal cultures by AAV1 viruses followed by detection of AMPA receptor subunits.

B Western blot analysis of total GluA1 expression in Ctrl or Fxr1 overexpression (Fxr1) condition during upscaling (Ctrl/Veh $n = 5$, Ctrl/TTX $n = 5$, Fxr1/Veh $n = 6$, Fxr1/Veh $n = 6$). One-way ANOVA with Dunnett's multiple comparison test $^{***}P < 0.001$.

C Western blot analysis of total GluA1 expression in Ctrl or Fxr1 over condition during downscaling (Ctrl/Veh $n = 4$, Ctrl/TTX $n = 4$, Fxr1/Veh $n = 4$, Fxr1/Veh $n = 4$).

D RT–qPCR measurement of Gria1 mRNA in Ctrl or Fxr1 over condition during upscaling (Ctrl/Veh $n = 3$, Ctrl/TTX $n = 3$, Fxr1/Veh $n = 3$, Fxr1/Veh $n = 3$). One-way ANOVA with Bonferroni's multiple comparison test $^{***}P < 0.001$.

E Schematic representation of tagging of luciferase cDNA with 5′UTR, 1–900CDS, 900–1,800CDS, 1,800–2,700CDS, and 3′UTR of GluA1 gene.

F Measurement of relative luciferase signal after co-transfection of different tagged luciferase constructs along with GFP (Ctrl) or GFP-Fxr1 (Fxr1) plasmids. $n = 5$ in each condition, Student's t-test $^{*}P < 0.05$, $^{***}P < 0.001$.

G Immunostaining for surface GluA1 in GFP (Ctrl) or GFP-Fxr1 (Fxr1 over)-infected cultures after treatment with Veh, TTX, or BIC for 48 h.

H Percentage of surface GluA1 relative to the mean of Ctrl/Veh condition (Ctrl condition: Veh $n = 63$, TTX $n = 34$, BIC $n = 29$, Fxr1 condition: Veh $n = 56$, TTX $n = 30$, BIC $n = 29$). One-way ANOVA with Bonferroni's multiple comparison test $^{*}P < 0.05$, $^{**}P < 0.01$, $^{***}P < 0.001$.

Data information: Error bars are ± SEM.
Source data are available online for this figure.

the presence of single (Fxr1 or Gsk3β) or double (Gsk3β and Fxr1) KO of targeted genes (Fig EV2E–H).

Whole-cell patch-clamp recordings showed a multiplicative increase in mEPSC amplitude in control neurons following upscaling (Figs 3A–D and O, and EV3). Fxr1 overexpression or Gsk3β KO prevented the increase in mEPSC amplitude induced by TTX (Figs 3E, F and O, and EV3).

The Fxr1 KO condition resulted in an elevation of mEPSC amplitude in a multiplicative manner (Figs 3G–J and O, and EV3) to a level that was not further increased following activity blockade by TTX (Figs 3G and O, and EV3). Similarly, the double Gsk3β/Fxr1 KO induced a multiplicative elevation of mEPSC amplitude (Figs 3K–N and O, and EV3) that was not further increased by TTX treatment (Figs 3K and O, and EV3). No changes in mEPSC frequency were observed in all conditions (Fig 3P).

Overall, these observations confirm that Fxr1 upregulation prevents upscaling and reveal that a decrease in Fxr1 protein is necessary and sufficient for the induction of this form of homeostatic plasticity. Furthermore, genetic inactivation of Gsk3β, which increases Fxr1 levels (Del'Guidice *et al*, 2015), also inhibits upscaling in an Fxr1-dependent manner. These findings are compatible with a mechanism by which Gsk3β is activated and negatively regulates Fxr1 protein level to contribute to upscaling.

Fxr1 modulates sleep duration and the response to sleep deprivation

We next investigated the involvement of Fxr1 in the homeostatic regulation of neuronal activity at the system level by verifying whether Fxr1 is involved in the regulation of sleep, which is homeostatically regulated. Forty-eight hours of EEG and electromyographic (EMG) recordings were performed in freely moving mice injected with AAV SYN GFP-Fxr1 (Del'Guidice *et al*, 2015) or the control AAV SYN GFP into the frontal cortex.

Homeostatic sleep pressure accumulates during wake and is thus higher following enforced wakefulness or sleep deprivation (SD). We performed baseline (undisturbed) recordings for 24 h, followed by a 24-h recording including a 6-h SD and 18 h of recovery (termed recovery recording). Measurement of the time spent in wakefulness (WAKE), slow-wave sleep (SWS), and paradoxical sleep (PS) indicated that Fxr1 overexpressing mice have a significantly different distribution of vigilant states over time in baseline, an effect that became more pronounced during the recovery recording (Figs 4A and EV4B). This included an increased time spent in SWS (decreased time spent in WAKE) during the active/dark period that was likely related to longer individual bouts of SWS rather than to more individual bouts (Fig EV4C and D). We computed the power spectra for WAKE, SWS, and PS during baseline and recovery (Fig 4B). When normalized to the Ctrl, we noticed significant differences in the alpha frequency band (8–11.75 Hz) during wakefulness only in the recovery recording (Fig 4C and D), which includes SD. Pronounced effects during recovery can be indicative of involvement of Fxr1 in the response to elevated homeostatic sleep pressure.

The time course of EEG delta activity during SWS and of EEG theta and alpha activity during WAKE was also examined during and after SD to further assess changes in sleep regulatory mechanisms (Figs 4E and F, and EV4E). SWS delta power increases with sleep pressure as found with SD, and then, it rapidly decreases during recovery sleep (Mang & Franken, 2015). Low alpha activity and high theta activity during WAKE were shown to importantly contribute to the homeostatic need for sleep (Vassalli & Franken, 2017). Moreover, a decreased alpha/theta ratio was shown to associate with daytime sleepiness (Cheung *et al*, 2018). First, we found an increase in alpha/theta ratio in Fxr1 overexpressing mice compared with controls starting from the onset of SD (Fig 4E). Second, after SD, delta power in early dark phase was reduced in Fxr1 overexpressing mice (Fig 4F). These observations of changes in EEG responses to SD under Fxr1 overexpression suggest a contribution to the homeostatic regulation of sleep.

Fxr1 protein expression is reduced by sleep deprivation

Given that Fxr1 overexpression impacts EEG activity in response to SD, we investigated whether Fxr1 is affected by SD. Mice were divided into two groups, one group was sleep-deprived at the onset of the light phase (SD group), while the other was left undisturbed in the home cage (S group). Prefrontal cortex from both groups was dissected at the same time (Fig 5A). SD induced an increase in synaptic p845 GluA1 (Fig 5B) with no changes in p880 GluA2 (Fig 5C) as previously reported (Vyazovskiy *et al*, 2008). Western blot analysis showed that SD decreases levels of Fxr1 in the prefrontal cortex (Fig 5D). No changes in Fmrp protein were found after SD (Fig 5E). SD induced a slight increase in mRNA of Fxr2 (Fig 5G) with no change in Fxr1 or Fmrp mRNAs (Fig 5F and H).

© 2020 The Authors

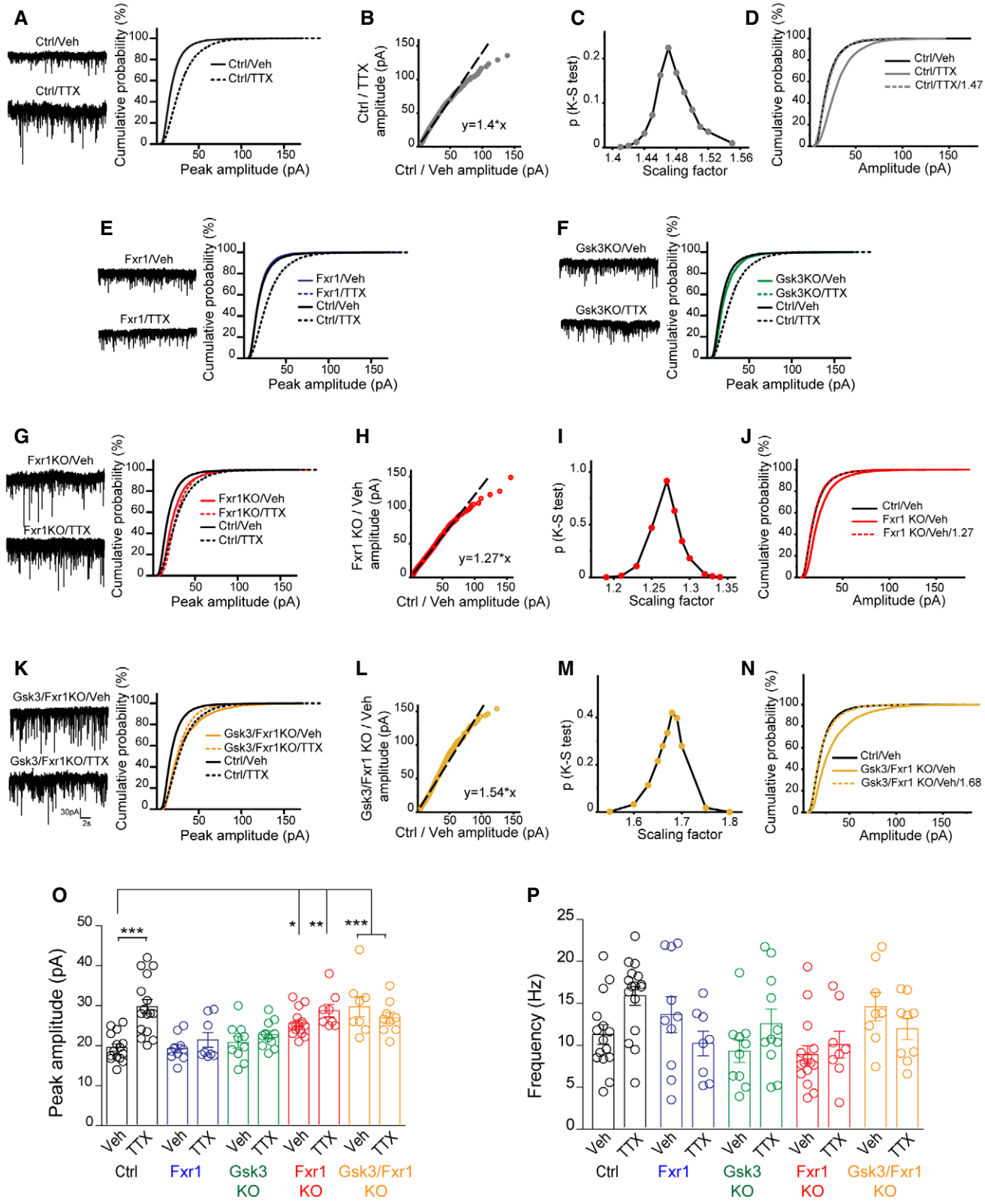

Figure 3.

© 2020 The Authors

Figure 3. The decrease in Fxr1 expression is necessary and sufficient for induction of multiplicative upscaling.

A Cumulative probability plots of mEPSC amplitude (500 events per cell) and representative examples of mEPSCs (left panel) recorded from cultured cortical control neurons after 48 h of 1 μM TTX or Veh exposure (Ctrl/Veh n = 16 and Ctrl/TTX n = 17).

B A linear fit of Ctrl/TTX and Ctrl/Veh amplitudes.

C The degrees of overlap between Ctrl/TTX and Ctrl/Veh data were assessed using various scaling factors. The largest nonsignificant P-value was obtained with 1.47 scaling factor.

D Cumulative probability plots of the mEPSC amplitude of Ctrl/Veh, Ctrl/TTX, and Ctrl/TTX divided by scaling factor 1.47, which yielded the maximum overlap with Ctrl/Veh data.

E–G Cumulative probability plots of mEPSC amplitude (500 events per cell) and representative examples of mEPSCs (left panel) recorded from cultured cortical neurons after 48 h of 1 μM TTX or Veh exposure, (E) Fxr1 overexpressing neurons (Fxr1/Veh n = 10 and Fxr1/TTX n = 8), (F) Gsk3 KO neurons (Gsk3KO/Veh n = 10 and Gsk3KO/TTX n = 11), (G) Fxr1 KO neurons (Fxr1KO/Veh n = 16 and Fxr1KO/TTX n = 8).

H A linear fit of Fxr1 KO/Veh and Ctrl/Veh amplitudes.

I The degrees of overlap between Fxr1 KO/Veh and Ctrl/Veh data were assessed using various scaling factors. The largest nonsignificant P-value was obtained with 1.27 scaling factor.

J Cumulative probability plots of the mEPSC amplitude of Ctrl/Veh, Fxr1 KO/Veh, and Fxr1 KO/Veh divided by scaling factor 1.27, which yielded the maximum overlap with Ctrl/Veh data.

K Cumulative probability plots of mEPSC amplitude (500 events per cell) and representative examples of mEPSCs (left panel) recorded from cultured cortical Gsk3 and Fxr1 KO neurons after 48 h of 1 μM TTX or Veh exposure (Gsk3/Fxr1KO/Veh n = 8 and Gsk3/Fxr1KO/TTX n = 11).

L A linear fit of Gsk3/Fxr1 KO/Veh and Ctrl/Veh amplitudes.

M The degrees of overlap between Gsk3/Fxr1 KO/Veh and Ctrl/Veh data were assessed using various scaling factors. The largest nonsignificant P-value was obtained with 1.68 scaling factor.

N Cumulative probability plots of the mEPSC amplitude of Ctrl/Veh, Gsk3/Fxr1 KO/Veh, and Gsk3/Fxr1 KO/Veh divided by scaling factor 1.68, which yielded the maximum overlap with Ctrl/Veh data.

O mEPSC mean amplitude of cultured cortical neurons after 48 h of 1 μM TTX or Veh exposure. One-way ANOVA with Bonferroni's multiple comparison test *P < 0.05, **P < 0.01, ***P < 0.001.

P mEPSC frequency of cultured cortical neurons after 48 h of 1 μM TTX or Veh exposure.

Data information: Error bars are ± SEM.

Overall, these results show that SD results in a reduction in Fxr1 protein expression (Fig 5), that is similar to what we observed following upscaling (Fig 1).

Fxr1 blocks increase in synaptic strength with sleep deprivation

It has been shown that SD results in an increase in mEPSCs (Liu *et al*, 2010). The level of Fxr1 protein is decreased by both synaptic upscaling (Fig 1) and SD (Fig 5). Furthermore, Fxr1 negatively regulates synaptic GluA1 during upscaling (Figs 2 and 3) and the EEG signature of SD (Fig 4). We thus examined whether Fxr1 and its negative regulator Gsk3β can block the increase in mEPSCs and synaptic GluA1 occurring following SD. To address this question, neuronal Fxr1 overexpression was achieved using AAV SYN GFP-Fxr1. A dual vector system involving AAV Gsk3sgRNA/GFP and AAV SpCas9 was used to achieve a neuron selective somatic KO (sKO) of Gsk3β (Khlghatyan *et al*, 2018).

Viral vectors were injected into the prefrontal cortex 3 weeks prior to SD (Fig 6A). Whole-cell patch-clamp recordings on brain slices confirmed that SD increases mEPSC amplitude in the cortex of control mice, infected with AAV SYN GFP (Fig 6B and E), as previously shown in nonviral vector-treated rodents (Liu *et al*, 2010). This effect was abolished following Fxr1 overexpression or Gsk3 sKO (Fig 6C–E). No changes were observed in mEPSC frequency in all the conditions (Fig 6F). Further characterization revealed a reduction in the rectification index following SD, indicating an increase in GluA1 containing calcium-permeable AMPA receptors in control mice (Fig 6G and H). Conversely, this effect of SD was again abolished in brain neurons overexpressing Fxr1 or lacking Gsk3β (Fig 6G and H). This indicates that augmentation of Fxr1 and inhibition of Gsk3β can prevent the increase in synaptic GluA1 during SD.

Neuronal translatome regulation by Fxr1 during sleep deprivation

We then aimed to investigate whether Fxr1 impacts the molecular response to SD. As an RNA-binding protein, Fxr1 has a large number of targets (Ascano *et al*, 2012). However, its neuron-specific targets have not been systematically characterized. This makes it difficult to pinpoint direct molecular effectors of Fxr1 during SD. Thus, we used conditional RiboTag-mediated RNA isolation (Sanz *et al*, 2009) and translatome sequencing to define the manner by which Fxr1 affects the molecular signature of SD.

RiboTag mice carry a ribosomal protein Rpl22 allele with a floxed wild-type (WT) C-terminal exon followed by an additional C-terminal exon with three hemagglutinin (HA) epitopes. Upon introduction of Cre recombinase, the WT C-terminal exon is replaced by the HA-tagged exon, which will allow immunoprecipitation of ribosomes and of associated RNA (Sanz *et al*, 2009). AAV-mediated introduction of Cre and Fxr1 to the RiboTag mouse brain allows isolating ribosome-associated RNAs only from cells that overexpress Fxr1. Moreover, unlike single cell or single nuclei techniques, this approach provides a large amount of mRNA with a better signal/noise ratio (Kronman *et al*, 2019) and preserves dendritic mRNA, which is important for local translation during plasticity.

RiboTag mice (Sanz *et al*, 2009) were infected with AAV SYN GFP-Fxr1 + AAV SYN Cre (Fxr1) or AAV SYN GFP + AAV SYN Cre (Ctrl) viruses 3 weeks prior to SD (Fig 7A). This allowed activating RiboTag in the same neurons that overexpress Fxr1 (Fig 7B and C). We found localization of GFP-tagged Fxr1 along dendrites in close proximity with HA-tagged ribosomes (Fig 7B) as previously reported for endogenous Fxr1 in cultured hippocampal neurons (Cook *et al*, 2011).

© 2020 The Authors

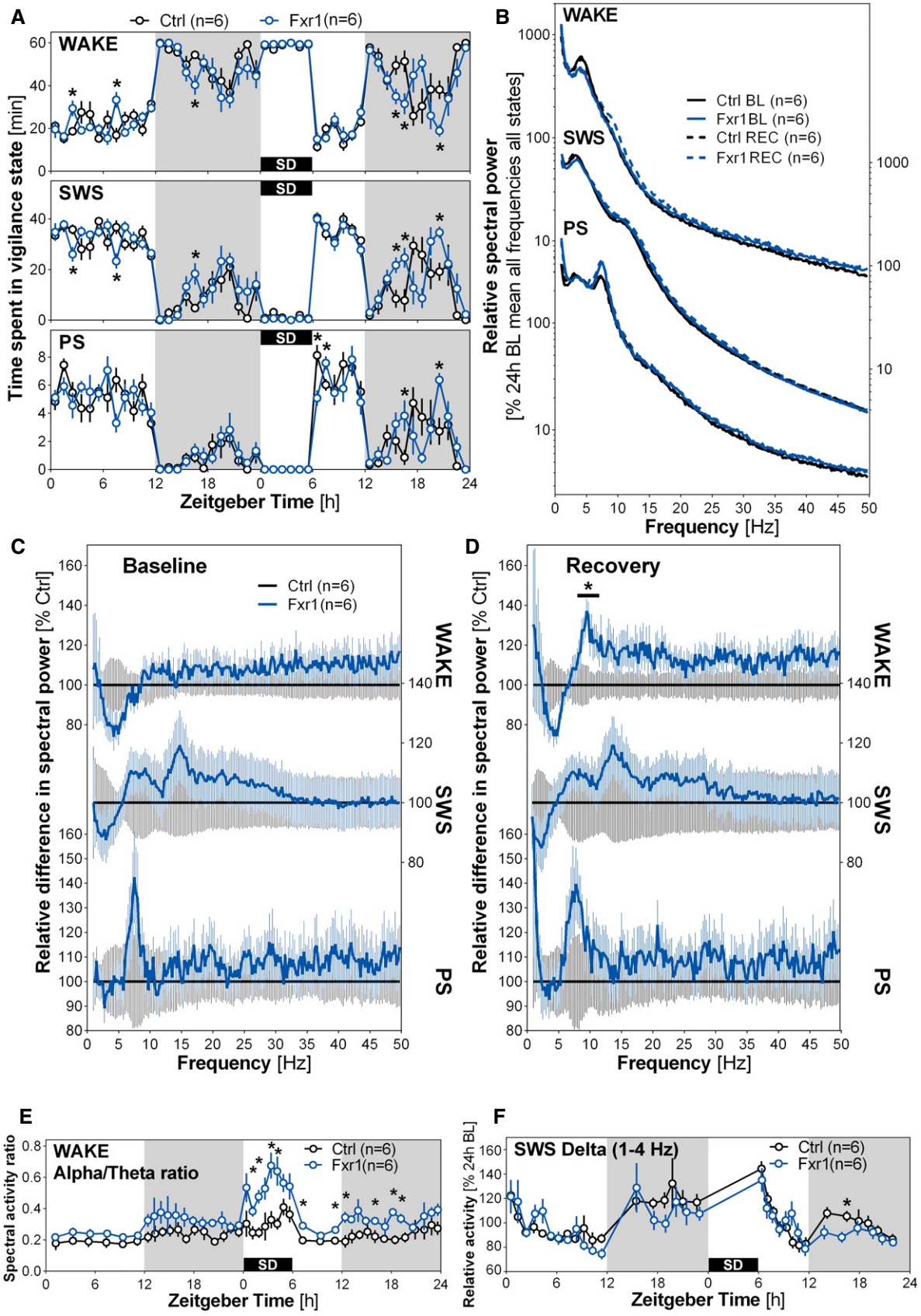

Figure 4.

© 2020 The Authors

Figure 4. Fxr1 modulates sleep duration and the response to sleep deprivation.

A Hourly distribution of wakefulness (WAKE), slow-wave sleep (SWS), and paradoxical sleep (PS) during a 24-h baseline (BL) recording and a second 24-h starting with 6-h sleep deprivation (SD) (recovery: REC) in Ctrl and Fxr1 overexpressing (Fxr1) mice. Significant group-by-hour interactions were found for wakefulness during BL ($F_{23,230}$ = 1.67, P = 0.046) and REC ($F_{23,230}$ = 2.83, P = 0.0029), for SWS during BL ($F_{23,230}$ = 1.66, P = 0.045) and REC ($F_{23,230}$ = 2.89, P = 0.0028), and for PS during REC ($F_{16,160}$ = 2.54, P = 0.0018, two-way ANOVA Huynh–Feldt-corrected, *P < 0.05).

B Power spectra for WAKE, SWS, and PS in Ctrl and Fxr1 mice computed between 0.75 and 50 Hz per 0.25-Hz for the full 24 h of BL and REC.

C, D The spectral activity of Fxr1 mice expressed relative to that of Ctrl mice for WAKE, SWS, and PS during (C) the 24-h BL and (D) the 24-h REC. A significant difference between groups was found for the frequency band 8–11.75 Hz during wakefulness (t = 2.30, P = 0.044 Student's t-test *P < 0.05).

E Time course of wakefulness spectral activity ratio between low alpha (8.5–10.5 Hz) and low theta (4–6 Hz) during BL and REC in Ctrl and Fxr1 mice. A significant group-by-interval interaction was found for REC ($F_{22,220}$ = 1.96, two-way ANOVA Huynh–Feldt-corrected; *P < 0.05) and also when using BL and REC intervals of the light periods ($F_{16,160}$ = 3.11, P < 0.01).

F Time course of SWS relative delta activity during BL and REC in Ctrl and Fxr1 mice. A significant group-by-interval interaction was found during REC ($F_{13,130}$ = 1.89, two-way ANOVA Huynh–Feldt-corrected; *P < 0.05).

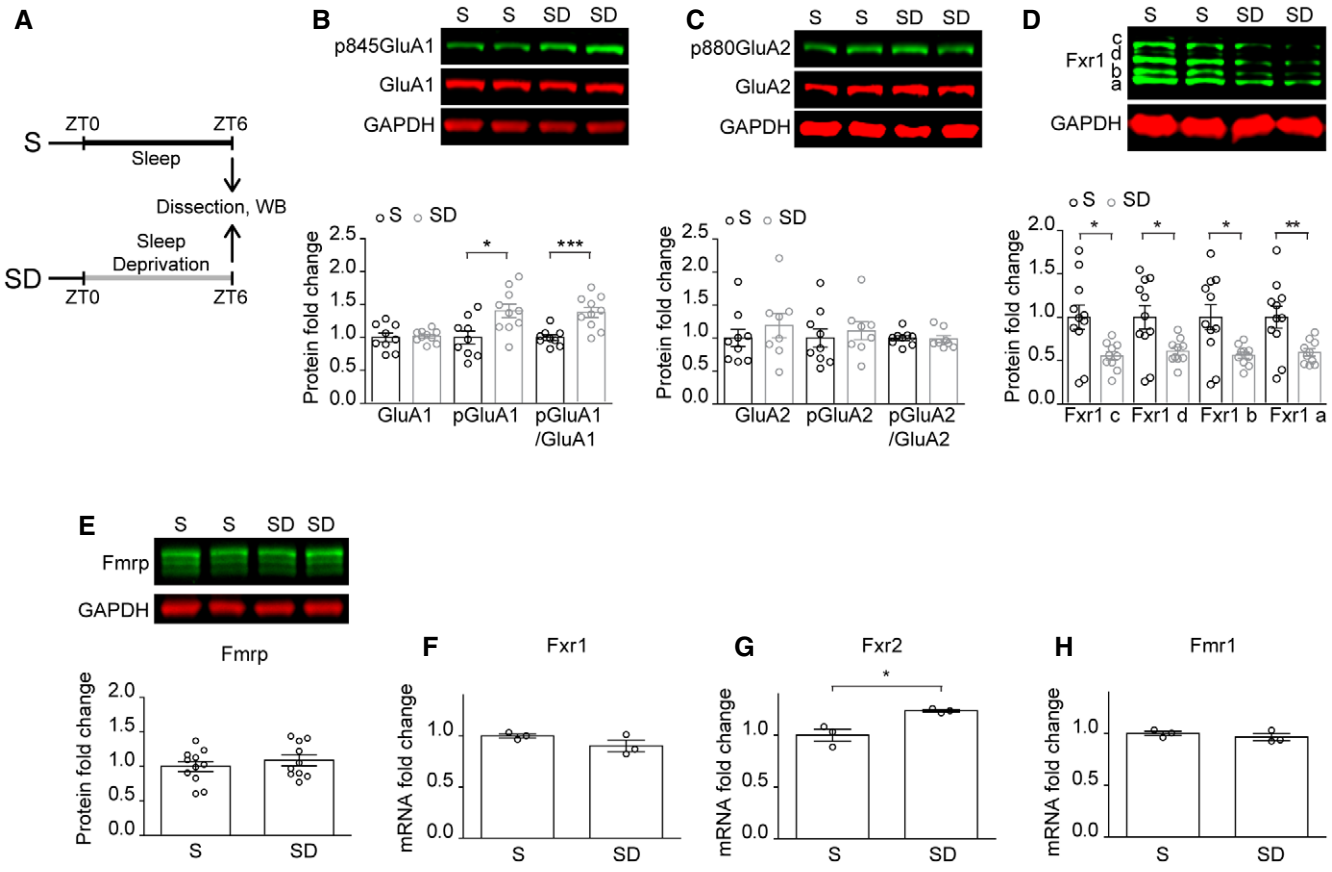

Figure 5. Fxr1 protein expression is decreased during sleep deprivation.

A Schematic representation of sleep deprivation (SD) experiments. Zeitgeber time 0 (ZT0) corresponding to lights ON.

B–E Western blot analysis of (B) p845GluA1 and GluA1 expression (S n = 9, SD n = 10), (C) p880GluA2 and GluA2 expression (S n = 9, SD n = 8), (D) Fxr1 expression (S n = 11, SD n = 10), and (E) Fmrp expression (S n = 11, SD n = 10) in the prefrontal cortex of sleeping and sleep-deprived mice. Student's t-test *P < 0.05, **P < 0.01, ***P < 0.001.

F–H RNAseq measurement of mRNA for (F) Fxr1, (G) Fxr2, and (H) Fmr1 during SD. n = 3 in each condition, Student's t-test *P < 0.05.

Data information: Error bars are ± SEM.
Source data are available online for this figure.

At the end of SD, RiboTag-associated RNAs were isolated and subjected to sequencing followed by pairwise comparison (Fig 7A) (GSE139576). We identified 2,401 unique differentially expressed transcripts (DETs) in Ctrl/S vs. Ctrl/SD comparison (Table EV1). Biological pathway enrichment (GO:BP; gProfiler) and clustering (EnrichmentMap and ClusterMaker in Cytoscape; Table EV4 (Reimand *et al*, 2019) revealed that 5 out of the 10 largest clusters have relationship with the synapse (protein localization in synapse, synaptic vesicle transport, dendrite spine morphogenesis, transport along microtubule, junction substrate adhesion) (Fig 7D). We thus

© 2020 The Authors

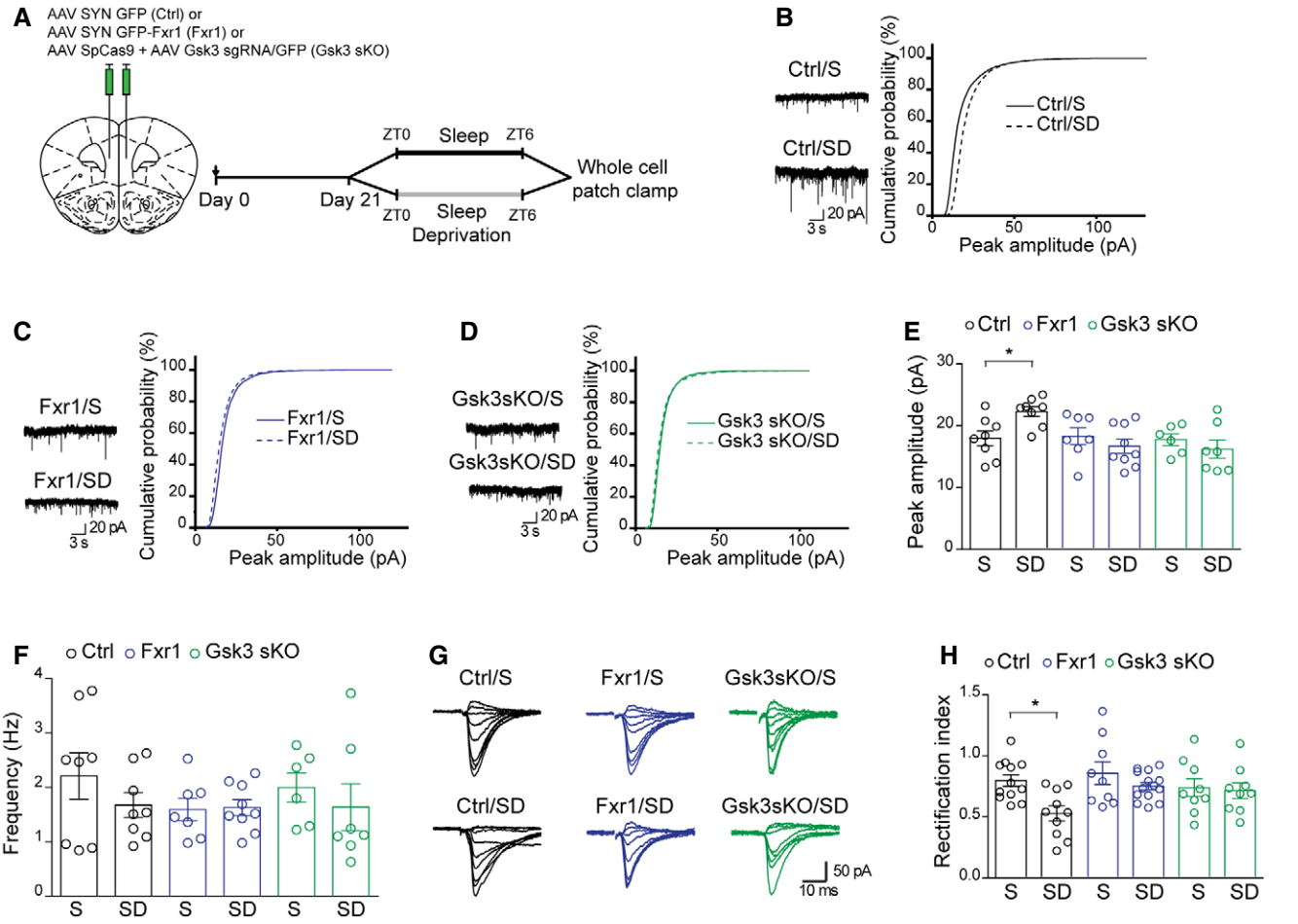

Figure 6. Fxr1 blocks increase in synaptic strength during sleep deprivation.

A Schematic representation of viral infection and sleep deprivation (SD) experiments. Zeitgeber time 0 (ZT0) corresponding to lights ON.

B–D Cumulative probability plots of mEPSC amplitude (500 events per cell) and representative examples of mEPSCs (left panel) recorded from brain slices of S and SD mice. (B) Control neurons (Ctrl/S n = 8 cells/4 mice and Ctrl/SD n = 8 cells/4 mice), (C) Fxr1 overexpressing (Fxr1/S n = 7 cells/5 mice and Fxr1 over/SD n = 9 cells/5 mice), and (D) Gsk3 sKO (Gsk3sKO/S n = 6 cells/3 mice and Gsk3sKO/SD n = 7 cells/4 mice).

E, F mEPSC (E) mean amplitude and (F) frequency of cortical neurons of S or SD mice. Control neurons (Ctrl/S n = 8 cells/4 mice and Ctrl/SD n = 8 cells/4 mice), Fxr1 overexpressing (Fxr1/S n = 7 cells/5 mice and Fxr1 over/SD n = 9 cells/5 mice), and Gsk3 sKO (Gsk3sKO/S n = 6 cells/3 mice and Gsk3sKO/SD n = 7 cells/4 mice). Student's t-test *$P < 0.05$.

G Representative examples of the current–voltage relationship of evoked EPSC amplitude recorded from S (top panel) and SD (bottom panel) mice.

H Summary bar graphs showing rectification index of control (S n = 12 cells/5 mice and SD n = 10 cells/5 mice), Fxr1P overexpressing (S n = 9 cells/4 mice and SD n = 14 cells/4 mice), and Gsk3 sKO (S n = 9 cells/3 mice and SD n = 9 cells/3 mice) neurons. One-way ANOVA with Bonferroni's multiple comparison *$P < 0.05$.

Data information: Error bars are ± SEM.

performed enrichment analysis using expert-curated and evidence-based synaptic gene ontology (SynGO) (Koopmans *et al*, 2019). This similarly indicated that SD-driven DETs (Ctrl/S vs. Ctrl/SD) are highly enriched for the synaptic localization, particularly for the postsynapse (Fig 7E, Table EV6). Moreover, functional enrichment indicated the involvement of those DETs in regulation of synapse organization, transport, metabolism, and synaptic signaling (Fig 7E, Table EV6).

Ctrl/SD vs. Fxr1/SD comparison identified 1,626 unique DETs (Table EV2), among which 241 transcripts were also affected by SD in Ctrl (Ctrl/S vs. Ctrl/SD overlap with Ctrl/SD vs. Fxr1/SD; Fig 7F, Table EV3). For most transcripts (232), Fxr1 overexpression reversed SD-induced changes (Fig 7G). These 232 transcripts were subjected to GO:BP enrichment and clustering, which revealed four enriched pathways (dense core vesicle transport, microtubule polymerization, cytoplasmic translation, and nucleosome DNA assembly; Fig 7H, Table EV5). Localization analysis by SynGO identified enrichment in the postsynaptic compartment (Fig 7I, Table EV7). SynGO functional analysis showed enrichment in synapse organization and metabolism (Fig 7I, Table EV7). This shows that during SD, Fxr1 is involved in the regulation of multiple synaptic processes such as local translation and regulation of synaptic structure (Fig 7E).

We then applied a more stringent cutoff for differential expression ($P < 0.001$), which identified 129 DETs between Ctrl/S and Ctrl/SD and 123 DETs between Ctrl/SD and Fxr1/SD, with the

 © 2020 The Authors

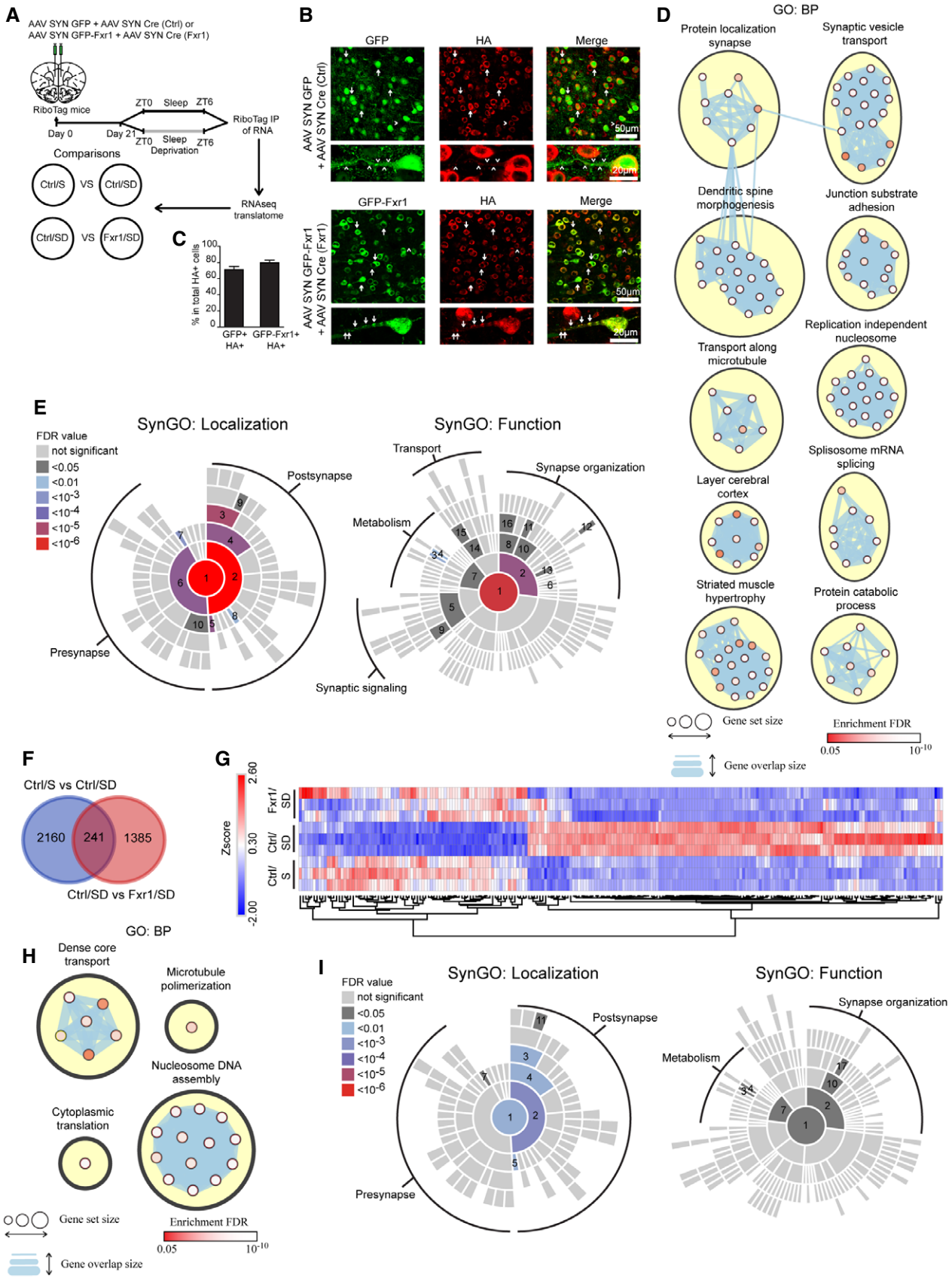
A
AAV SYN GFP + AAV SYN Cre (Ctrl) or
AAV SYN GFP-Fxr1 + AAV SYN Cre (Fxr1)
RiboTag mice
ZT0 Sleep ZT6
Day 0
Day 21
ZT0 Sleep ZT6
Deprivation
RiboTag IP of RNA
Comparisons
Ctrl/S VS Ctrl/SD
Ctrl/SD VS Fxr1/SD
RNAseq translatome
B
GFP
HA
Merge
AAV SYN GFP + AAV SYN Cre (Ctrl)
GFP-Fxr1
AAV SYN GFP-Fxr1 + AAV SYN Cre (Fxr1)
50µm
20µm
C
% in total HA+ cells
GFP+ HA+
GFP-Fxr1+ HA+
D
GO: BP
Protein localization synapse
Synaptic vesicle transport
Dendritic spine morphogenesis
Junction substrate adhesion
Replication independent nucleosome
Transport along microtubule
Splisosome mRNA splicing
Layer cerebral cortex
Striated muscle hypertrophy
Protein catabolic process
Gene set size
Gene overlap size
Enrichment FDR
0.05
10-10
E
SynGO: Localization
SynGO: Function
FDR value
not significant
<0.05
<0.01
<10-3
<10-4
<10-5
<10-6
Postsynapse
Presynapse
Transport
Synapse organization
Metabolism
Synaptic signaling
F
Ctrl/S vs Ctrl/SD
2160
241
1385
Ctrl/SD vs Fxr1/SD
G
Zscore
2.60
0.30
-2.00
Fxr1/SD
Ctrl/SD
Ctrl/S
H
GO: BP
Dense core transport
Microtubule polimerization
Nucleosome DNA assembly
Cytoplasmic translation
Gene set size
Gene overlap size
Enrichment FDR
0.05
10-10
I
SynGO: Localization
SynGO: Function
FDR value
not significant
<0.05
<0.01
<10-3
<10-4
<10-5
<10-6
Postsynapse
Presynapse
Synapse organization
Metabolism

Figure 7.

Figure 7. Neuronal translatome regulation by Fxr1 during sleep deprivation.

A Schematic representation of the experimental design. Zeitgeber time 0 (ZT0) corresponding to lights ON.
B Immunostaining for GFP and HA in Ctrl and Fxr1 mouse brain slices. Arrows indicate presence and arrowheads indicate an absence of GFP-tagged Fxr1 granules.
C Quantification of colocalization of GFP and HA-labeled neurons (GFP+HA+ 71.3% ± 3.7, n = 3, GFP-Fxr1+HA+ 79.7% ± 2.8, n = 3).
D Enrichment of differentially expressed transcripts from Ctrl/S vs. Ctrl/SD comparison in GO:BP. Top 10 clusters with the most number of enriched pathways (nodes) are shown.
E SynGO enrichment for synaptic localization and function of differentially expressed transcripts from Ctrl/S vs. Ctrl/SD comparison.
F Venn diagram showing overlap of differentially expressed transcripts between Ctrl/S vs. Ctrl/SD and Ctrl/SD vs. Fxr1 overexpression (Fxr1)/SD comparisons.
G Heat map showing transcripts that have bidirectional expression changes between Ctrl/S, Ctrl/SD, and Fxr1/SD conditions.
H Enrichment of commonly affected transcripts between Ctrl/S vs. Ctrl/SD and Ctrl/SD vs. Fxr1/SD comparisons in GO:BP.
I SynGO enrichment for synaptic localization and function of commonly affected transcripts between Ctrl/S vs. Ctrl/SD and Ctrl/SD vs. Fxr1 over/SD comparisons.

Data information: SynGO localization: 1—synapse, 2—postsynapse, 3—postsynaptic density, 4—postsynaptic specialization, 5—postsynaptic ribosome, 6—presynapse, 7—presynaptic ribosome, 8—postsynaptic cytosol, 9—postsynaptic density intracellular compartment, 10—presynaptic active zone, 11—integral component of postsynaptic density membrane. SynGO function: 1—process in the synapse, 2—synapse organization, 3—protein translation at presynapse, 4—protein translation at postsynapse, 5—trans-synaptic signaling, 6—synapse adhesion between pre- and postsynapse, 7—metabolism, 8—structural constituent of synapse, 9—chemical synaptic transmission, 10—synapse assembly, 11—regulation of synapse assembly, 12—regulation of modification of postsynaptic actin cytoskeleton, 13—postsynaptic cytoskeleton organization, 14—axo-dendritic transport, 15—dendritic transport, 16—structural constituent of postsynapse, 17—postsynaptic specialization assembly.

overlap comprising 14 DETs (Fig EV5A and B). Since these 14 DETs can be a small part of a larger network, we used the GeneMANIA algorithm to identify their known interacting partners. This algorithm finds 20 known interaction partners for each transcript (or a protein coded by a given transcripts) and constructs the smallest possible network by finding common interaction partners for a given list of transcripts. Application of the GeneMANIA algorithm to 14 DETs resulted in a network consisting of just 33 members (Fig EV5C). This indicated that those 14 DETs are highly interconnected into a small network (less connectedness would result in a higher number of genes, maximum $14 \times 20 = 340$). Interestingly, a majority of these interactions occur at a protein level (physical interaction, 60.5%) (Fig EV5C), suggesting that those 14 DET are functionally relevant for the regulation of molecular networks that are not directly obvious from the analysis of ribosome-associated mRNAs.

Enrichment analysis on this interconnected network revealed three major themes: regulation of synaptic structure, signal transduction, and serine/threonine phosphorylation (Fig EV5D and E). Members of this network include key players of structural synaptic plasticity (Camk2, Rac1, Cdc42, Pak1, Pak3, Tiam1) (Woolfrey & Srivastava, 2016; Fu & Ip, 2017) that represents hotspots of significant regulation during homeostatic scaling (Schanzenbacher *et al*, 2016). Overall, this suggests that Fxr1 regulates transcripts involved in structural synaptic plasticity, which can be underlying its shared contribution to SD and scaling.

Discussion

Homeostatic regulation of synaptic strength necessitates both cell-autonomous and system-level mechanisms. Here, we show that the insomnia GWAS-associated gene *Fxr1* encodes a protein involved in the regulation of synaptic strength during cell-autonomous synaptic scaling and synchronized EEG activity response to an increased homeostatic sleep need. Fxr1 expression is downregulated by both upscaling and SD. Furthermore, manipulations of Fxr1 and its negative regulator Gsk3β contribute to changes in GluA1 localization and mEPSC amplitude following upscaling and SD. Translatome sequencing is indicating that Fxr1 regulates transcripts related to local protein synthesis and synaptic structure during SD. Based on our findings, we propose that during upscaling and elevated homeostatic sleep pressure, Fxr1 protein level decreases due to its negative regulation by Gsk3β (Del'Guidice *et al*, 2015; Qie *et al*, 2017); this decrease in Fxr1 protein induces several alterations in synaptic organization, which includes an increase in synaptic GluA1 and in postsynaptic excitatory activity.

We have shown that Fxr1 protein levels are only affected during upscaling and not downscaling. In line with this, Fxr1 overexpression affected surface and total GluA1 expression only during upscaling and not during downscaling or under basal conditions. Most importantly, Fxr1 overexpression abolished upscaling, while decreasing Fxr1 was sufficient to induce upscaling. This shows that Fxr1 downregulation is a necessary and sufficient mechanism inducing upscaling, thus underscoring the role of Fxr1 as a selective master regulator of this form of homeostatic plasticity. Furthermore, Fxr1 overexpression affected mEPSCs only during upscaling or SD, and had no effect on basal mEPSCs *in vitro* and *in vivo*. Thus, the regulation of synaptic GluA1 by Fxr1 appears to be specifically engaged in response to external conditions, supporting its contribution to homeostatic responses.

Fmrp has previously been shown to be involved in the homeostatic regulation of synaptic strength by retinoic acid (Soden & Chen, 2010). However, a lack of Fmrp expression abolishes upscaling in this system (Soden & Chen, 2010) and our results show that Fmrp protein levels are not affected by upscaling. In contrast, Fxr1 is downregulated in response to TTX, and Fxr1 KO is sufficient to induce upscaling, while Fxr1 overexpression prevents this form of homeostatic plasticity. Differences in the contributions of Fxr1 and Fmrp can be partially explained by the mode of regulation of synaptic GluA1 subunit by these two proteins. Fmrp has been shown to facilitate GluA1 delivery to the membrane (Guo *et al*, 2015), while our results show that Fxr1 blocks this process during upscaling. Similar to Fmrp, Fxr2 also positively regulates GluA1 albeit, via stabilization of its mRNA (Guo *et al*, 2015). Nevertheless, the role of Fxr2 in synaptic scaling has not been investigated. Overall, the downregulation of Fxr1 by upscaling and the negative role of Fxr1 in regulating synaptic GluA1 point to different contributions of the members of the fragile X family proteins in the regulation of forms of homeostatic plasticity.

 © 2020 The Authors

Fxr1 expression was not affected by downscaling, and Fxr1 overexpression did not affect downscaling or EEG activity during undisturbed/normal sleep. Fxr1 overexpression specifically affected upscaling and EEG activity during WAKE and SWS in response to SD. This suggests a very specific contribution of Fxr1 in the response to an homeostatic sleep challenge that could match its role in homeostatic plasticity. Upscaling occurring as a result of visual deprivation was shown to take place specifically during wakefulness (Hengen *et al*, 2016), while downscaling appears to be mostly happening with sleep (Diering *et al*, 2017). Our study indicates that the regulator of homeostatic upscaling Fxr1 contributes to the wake EEG response to sleep deprivation, which could point to a role in sleep homeostasis.

In particular, wakefulness alpha activity was specifically increased by Fxr1 overexpression under sleep-deprived conditions, together with the alpha/theta ratio. Less than 10-Hz activity and alpha (8–12 Hz) activity are features of quiet wakefulness that are decreasing during active wakefulness characterized by locomotion or somatosensory stimulation (Infarinato *et al*, 2015; McGinley *et al*, 2015). Wakefulness alpha has been proposed to either serve the processing of task-relevant information or filter out irrelevant information in rodents and humans (Broussard & Givens, 2010; Vijayan & Kopell, 2012; van Diepen *et al*, 2016). Increased wake alpha under Fxr1 overexpression could thus functionally impact information processing (during rest) under elevated homeostatic sleep pressure. Interestingly, alpha activity was shown to positively correlate with glutamate level (Arrubla *et al*, 2017) and to be genetically linked to glutamate transmission (Salmela *et al*, 2016).

Our results revealed that changes to the translatome occurring with SD are modulated by Fxr1. This effect of Fxr1 may contribute to alterations in alpha activity in addition to changes in synaptic strength both specifically observed after SD. In particular, elements linked to SD-associated (structural) plasticity, such as CamK2 (Areal *et al*, 2017), are of particular relevance to act on both the neuronal and EEG levels. GeneMANIA analysis of interactions indicated that DETs affected by Fxr1 overexpression in the context of SD belong to a signaling network implicated in structural synaptic plasticity. It has been shown that neuronal activity results in local calcium changes that modulate activation of Camk2. This results in changes in activity of small Rho GTPases Rac1 and Cdc42 that in turn act on downstream effectors such as Pak1 and Pak3 to regulate actin dynamics during dendritic spine plasticity (Woolfrey & Srivastava, 2016; Fu & Ip, 2017). Activity of Rac1 and Cdc42 has been shown to be regulated by guanine exchange factors (GEFs) such as Tiam1. Recent proteomic study found that the regulation of Rho GTPases (Rac1, Cdc42) and dendritic morphology regulator Tiam1 (Woolfrey & Srivastava, 2016; Fu & Ip, 2017) represents a key regulation hub during homeostatic scaling (Schanzenbacher *et al*, 2016). Even if we cannot exclude that parts of the SD-driven changes could be due to stimulation (enriched wake) following exposure to a clean cage within our SD procedure (Raven *et al*, 2018), we believe that the effects of Fxr1 on the response of the translatome to SD are matching its role in homeostatic plasticity and could contribute to the observed electrophysiological modifications.

The mechanisms by which Fxr1 is downregulated in both SD and upscaling necessitate Gsk3β activity and a downregulation of Fxr1 protein level. Fxr1 has been shown to be phosphorylated by Gsk3β and targeted for degradation following its ubiquitination (Del'Guidice *et al*, 2015; Qie *et al*, 2017). However, this regulation involves the priming of Fxr1 by other kinases and may thus integrate information from several upstream signaling pathways (Del'Guidice *et al*, 2015). Similarly, Fxr1 also regulates the translation, trafficking, and stability of several mRNA (Whitman *et al*, 2011; Ascano *et al*, 2012; El Fatimy *et al*, 2016). In the context of SD, our results indicate that the translation of multiple transcripts involved in neuronal processes including synapse organization and metabolism are regulated, directly or not, by Fxr1 in the prefrontal cortex. Taken together, these observations suggest that the Gsk3β-Fxr1 module may constitute a shared signaling hub involved in the homeostatic regulation of synaptic strength both at the cell autonomous and system level in response to environmental-allostatic loads such as SD (McEwen, 2012; McEwen & Karatsoreos, 2015).

The contribution of Fxr1 to both the homeostatic regulation of synaptic strength and the regulation of sleep can be important for understanding the pathophysiology of several human disorders. Indeed, variants in the Fxr1 locus have been GWAS-associated with insomnia (Jansen *et al*, 2019) and mental illness including schizophrenia and bipolar disorder (Ripke *et al*, 2014; Liu *et al*, 2016). Fxr1 is also differentially expressed in the brain of people with schizophrenia (Brodl *et al*, 2018), while a schizophrenia-associated SNP in *FXR1* has been linked to self-reported sleep duration (Dashti *et al*, 2019). The interaction between *Fxr1* and *Gsk3b* has also been reported to affect anxiety-related behaviors in mice (Khlghatyan *et al*, 2018) and self-reported emotional stability in humans (Del'Guidice *et al*, 2015). Furthermore, the expression of Fxr1 can be regulated by lithium and other mood-stabilizing drugs as a consequence of Gsk3 inhibition (Beaulieu *et al*, 2009; Del'Guidice *et al*, 2015). Neuropsychiatric disorders and lithium have been associated with regulation/dysregulation of sleep (Billiard, 1987; Picchioni *et al*, 2014) and of homeostatic plasticity (Wondolowski & Dickman, 2013; Gideons *et al*, 2017; Kavalali & Monteggia, 2020; Tatavarty *et al*, 2020). Further investigations of the Gsk3β-Fxr1 signaling module should clarify whether it also constitutes a molecular link between mental illnesses, sleep homeostasis, and cell-autonomous homeostatic plasticity.

Materials and Methods

Experimental model and subject details

All experiments conducted in this study are approved by the Université Laval, the CIUSSS-NIM, and the University of Toronto Institutional Animal Care Committees in line with guidelines from the Canadian Council on Animal Care.

Experimental animals

For primary cultures, postnatal day 0–day 1 (P0–P1) pups of C57BL/6J mice were used. For stereotaxic injection followed by ribosome immunoprecipitation (RiboTag IP), 3- to 4-month-old RiboTag mice (Sanz *et al*, 2009) were used. For all other experiments, C57BL/6J male (Jackson Laboratory, Bar Harbor, ME) mice were used. Littermates were housed 3–4 per cage in a humidity-controlled room at 23°C on a 12-h light–dark cycle with *ad libitum* access to food and water. At the time of experiment, mice were 3–4 months old and

© 2020 The Authors

weighed approximately 25–30 g. All animals were used in scientific experiments for the first time. This includes no previous exposures to pharmacological substances or altered diets.

Primary cultures

Primary cortical cultures were prepared from P0 to P1 C57BL/6J mouse pups as described (Swift *et al*, 2011). Briefly, neurons were dissociated from cortices of P0–1 pups and seeded on poly-D-lysine-coated coverslips (Neuvitro, Vancouver, WA) in 24-well plates. For Western blot analysis and electrophysiology, neurons were seeded at the density of 5×10^5 cells per well. For surface expression analysis, neurons were seeded at the density of 1.5×10^5 cells per well. Cultures were grown at 37°C and 5% CO_2 in Neurobasal plus medium, supplemented with B27 plus, GlutaMAX (Thermo Fisher Scientific, Waltham, MA), and penicillin/streptomycin mix for a total of 13–14 days.

DNA constructs

To knockout (KO) *Fxr1* gene, 20-nt target sequences in exons of this gene were selected using online CRISPR design tool (http://crispr.mit.edu/) to minimize off-target activity. For *in vitro* testing, guide oligonucleotides (targeting *Fxr1*) were cloned into pX330 (pX330-U6-Chimeric_BB-CBh-hSpCas9 was a gift from Feng Zhang (Addgene # 42230)) (Cong *et al*, 2013) all in one vector by single-step cloning using BbsI restriction sites (Ran *et al*, 2013).

For primary neuronal culture, transfection previously characterized Gsk3b gRNA oligonucleotide (Khlghatyan *et al*, 2018) was cloned into pX458 (pSpCas9(BB)-2A-GFP (PX458) was a gift from Feng Zhang (Addgene plasmid # 48138)) (Ran *et al*, 2013) vector by single-step cloning using BbsI restriction sites to generate Gsk3 KO construct. pX458 vector was used as a control (Gsk3 Ctrl construct). To generate Fxr1 Ctrl construct, first GFP from pX458 vector was changed to mCherry. mCherry was PCR-amplified by forward (mCherryF) 5′-AATAATGAATTCGGCAGTGGAGAGGGCAGAGGAAGTCTGCTAACATGCGGTGACGTCGAGGAGAATCCTGGCCCAGTGAGCAAGGGCGAGGAGGATAACA-3′ and reverse (mCherryR) 5′-AATAATGAATTCTTACTTGTACAGCTCGTCCATGC-3′ primers and in serted into the pX458 vector using EcoRI restriction sites. To generate the Fxr1 KO construct, the most active *Fxr1* targeting guide (Fxr1 gRNA2) oligonucleotide was cloned into Fxr1 Ctrl vector by single-step cloning using BbsI restriction sites.

For *in vitro* KO of *Fxr1* in Fig EV2, guide was cloned into pX459 vector (pSpCas9(BB)-2A-Puro (PX459) V2.0 was a gift from Feng Zhang (Addgene plasmid # 62988)) (Ran *et al*, 2013). Sequences of all constructs were verified.

AAV viral particle preparation

AAV serotype 1 SYN GFP-Fxr1 viral particles were produced by the University of North Carolina (UNC) Vector Core Facility. AAV serotype 5 SpCas9, Gsk3sgRNA/GFP, and SYN GFP-Fxr1 are previously characterized (Khlghatyan *et al*, 2018) and are also produced by the University of North Carolina (UNC) Vector Core Facility. AAV serotype 1 GFP (AAV1 SYN GFP), AAV serotype 5 GFP (AAV5 SYN GFP), and AAV serotype 5 Cre (AAV5 SYN Cre) were purchased from Addgene.

Cell line culture and transfection

Neuro-2A (N2A) cells were grown in high-glucose DMEM containing 10% FBS, penicillin/streptomycin, and L-glutamine (HyClone-GE Healthcare, Logan, UT). Cells were maintained at 37°C in 5% CO_2 atmosphere and transfected using Lipofectamine 2000 (Thermo Fisher Scientific, Waltham, MA) according to the manufacturer's protocols.

To test the activity of Fxr1 sgRNA by Western blot (Fig S3F), 50–70% confluent N2A cells were transfected with all in one px459-based constructs (pX459 vectors with guide targeting *Fxr1*). To select only transfected cells, 48 h after transfection cells were incubated with 3 μM puromycin for 72 h followed by 48 h of incubation without puromycin. Cells were washed and lysed on day 7 after transfection.

Genomic DNA extraction and SURVEYOR assay

For functional testing of sgRNAs, 50–70% confluent N2A cells were transfected with all in one pX330-based constructs (pX330 vectors with guides targeting *Fxr1*). Cells transfected with pX330 only served as a negative control. Cells were lysed 48 h after transfection by tail buffer (Tris pH = 8.0 0.1 M, NaCl 0.2 M, EDTA 5 mM, SDS 0.4%, and proteinase K 0.2 mg/ml), and DNA was precipitated using isopropanol followed by centrifugation (13,000 *g*, 15 min). DNA was resuspended in TE Buffer (10 mM Tris pH 8.0, 0.1 mM EDTA) and used for downstream analysis. Functional testing of individual sgRNAs was performed by SURVEYOR nuclease assay (Transgenomics, Omaha, NE) using PCR primers listed below. Band intensity quantification was performed as described (Ran *et al*, 2013).

PCR primers used in the SURVEYOR assay:

Gene exon	Forward primer sequence	Reverse primer sequence
Fxr1 exon 4	GAGCAGTGTTGGCACATGTTAT	CGGTGTTCTAGAATCCCCTCT
Fxr1 exon 8	TGCCACTTTCCTCTTTTGGTG	AAGCCTGTCCTCCTAACGAC
Fxr1 exon 10	AAGCTGTGTCTACCAGGATCA	TCAAACGTGACGAATGGGCT

Primary cortical culture transfection and infection

Cultures were transfected at DIV7 (with Gsk3 Ctrl, Gsk3 KO, Fxr1 Ctrl, Fxr1 KO constructs) and at DIV10 (with Fxr1 overexpression construct) using DNA In-Neuro transfection (MTI-GlobalStem, Gaithersburg, MA) reagent according to manufacturer's protocols. Cultures were infected at DIV5 with AAV1 SYN GFP or AAV1 SYN GFP-Fxr1. Viruses were added to the cultures at the titer of 2×10^4 viral genomes (Vg)/per neuron.

To induce upscaling or downscaling, cells were incubated in the presence of 1 μM TTX or 50 μM BIC (Alomone Labs, Jerusalem, Israel) or vehicle, respectively, from DIV12 to DIV14. All experiments were performed at DIV14.

Stereotaxic injections

Three weeks before the SD and electrophysiology recordings, bilateral injection of the virus was made in the prefrontal cortex. Mice were anesthetized with a preparation of ketamine 10 mg/ml and

 © 2020 The Authors

xylazine 1 mg/ml (0.1 ml/10 g, i.p.). The animal was placed in a stereotaxic frame, and the skull surface was exposed. Two holes were drilled at injection sites, and 1 μl of virus (AAV GFP-Fxr1 4.4×10^{12} vg/ml or AAV GFP 4.5×10^{12} vg/ml or 1:1 AAV mixture: AAV SpCas9 2.6×10^{12} vg/ml and AAV Gsk3sgRNA/GFP 5.4×10^{12} vg/ml or AAV SpCas9 and AAV GFP 4.5×10^{12} vg/ml, AAV SYN GFP-Fxr1 4.4×10^{12} vg/ml and AAV SYN Cre 5.5×10^{12} vg/ml or AAV SYN GFP 4.5×10^{12} vg/ml and AAV SYN Cre 5.5×10^{12} vg/ml) was injected using nanoliter injector with microsyringe pump controller (WPI) at the speed of 4 nl per second. Following coordinates were used: anterior–posterior (AP), +2.4 mm anterior to bregma; mediolateral (ML), ± 0.5 mm; and dorsoventral (DV), 1.7 mm below the surface of the brain. All measures were taken before, during, and after surgery to minimize animal pain and discomfort.

Surgeries for EEG recordings

The surgery combined viral delivery to the frontal cortex with electrode implantation for EEG/EMG recording that has been performed as described previously (El Helou *et al*, 2013; Freyburger *et al*, 2016; Seok *et al*, 2018). Mice were anesthetized (ketamine/xylazine 120/10 mg/kg, intraperitoneal injection) and placed in a stereotaxic frame. A 28-gauge cannula was positioned for injection to the right frontal cortex (1.5 mm anterior to bregma, 1.5 mm lateral to midline, and 1.5 mm below the skull surface) and delivered 1 μl of AAV GFP (4.7×10^{12} vg/ml) or of AAV-Fxr1-GFP (4.4×10^{12} vg/ml) at an injection speed of 0.025 μl/min. The cannula was left in place for 5 min after the injection and then slowly removed. Two gold-plated screws (EEG electrodes; diameter 1.1 mm) were screwed through the skull over the right cerebral hemisphere: the first above the AAV injection site and the second above the posterior cortex (1 mm anterior to lambda, 1.5 mm lateral to the midline). An additional screw serving as a reference electrode was implanted on the right hemisphere (0.7 mm posterior to bregma, 2.6 mm lateral to the midline) together with three anchor screws implanted on the left hemisphere. Two gold wires were implanted between neck muscles and served as EMG electrodes. Electrodes were soldered to a connector and fixed to the skull with dental cement. Four days after surgery, mice were connected to a swivel relay and habituated to the cabling condition until recording.

EEG recording and analyses

EEG/EMG recording and analyses were performed similarly to previously described (El Helou *et al*, 2013; Freyburger *et al*, 2016; Seok *et al*, 2018). Briefly, signals were amplified with Lamont amplifiers, and sampled at 256 Hz and filtered using the software Stellate Harmonie (Natus, San Carlos, CA). A bipolar montage was used for the visual identification of vigilance states [wakefulness, slow-wave sleep (SWS), paradoxical sleep (PS)] on 4-s epochs, and the time spent in each state was computed per hour as well as per 12-h light and dark periods. Spectral analysis was computed using fast Fourier transform on artifact-free epochs of the anterior/frontal EEG signal (referenced to the reference electrode) to calculate spectral power per 0.25-Hz bins from 0.75 to 50 Hz and per frequency bands [i.e., SWS delta (1–4 Hz), wakefulness low theta (4–6 Hz), and low alpha (8.5–10.5 Hz)]. Power spectra were normalized relative to the total power of all states during baseline and also subsequently as a function of spectral activity in the control group. The spectral activity of frequency bands was averaged for intervals containing an equal number of SWS or wakefulness epochs and expressed relative to 24-h baseline mean as described before (Curie *et al*, 2013; El Helou *et al*, 2013; Freyburger *et al*, 2016). More precisely, to take into account the distribution of wakefulness and SWS, SWS delta activity was average for 12 equal intervals during the baseline light period, six equal intervals during the dark periods, and eight equal intervals during the 6-h light period following SD, whereas wakefulness low theta activity and low alpha activity were averaged for six equal intervals during the baseline light period, 12 equal intervals during dark periods, eight equal intervals during SD, and three equal intervals during the 6-h light period following SD. A frequency band activity ratio was computed by dividing low alpha by low theta absolute activity separately for each interval. The distribution of vigilance states and the time course of activity in frequency bands have been plotted according to Zeitgeber time (Zeitgeber time 0 = Lights ON; Zeitgeber time 12 = Lights OFF).

Statistical analyses for EEG recordings

Hourly distribution of vigilance state duration, time spent in vigilance states computed per 12-h periods, average duration of vigilance state individual bouts per 12-h periods, number of individual bouts of vigilance state per 12-h periods, and time course of spectral activity in frequency bands have been compared between groups (Ctrl vs. Fxr1 overexpression) using two-way repeated-measure analyses of variances (ANOVAs). Significance levels were adjusted for repeated measures using the Huynh–Feldt correction, and significant interactions were decomposed using planned comparisons. Spectral activity in the alpha band during wakefulness was compared between groups using *t*-tests. The threshold for statistical significance was set to 0.05, and data are presented as the mean and standard error of the mean.

Acute slice preparation

Mice were taken for experiments 6 h after the onset of the light phase with or without SD. Mice were killed by rapid cervical dislocation. Cortical slices (300 μm) were prepared from mice (3 weeks after injection of viruses) using a vibrating-blade microtome (Leica Biosystem, Wetzlar, Germany). Slices were prepared using ice-cold artificial cerebrospinal fluid (ACSF) containing NaCl 87 mM, $NaHCO_3$ 25 mM, KCl 2.5 mM, NaH_2PO_4 1.25 mM, $MgCl_2$ 7 mM, $CaCl_2$ 0.5 mM, glucose 25 mM, and sucrose 75 mM. Right after sectioning, slices were placed in oxygenated ACSF at 32°C for 30 min, transferred to extracellular ACSF, and maintained at room temperature prior to experiments. All recordings were performed with extracellular ACSF containing NaCl 124 mM, $NaHCO_3$ 25 mM, KCl 2.5 mM, $MgCl_2$ 1.5 mM, $CaCl_2$ 2.5 mM, and glucose 10 mM, equilibrated with 95% O_2/5% CO_2, pH 7.4, maintained at 31–33°C, and perfused at a rate of 2–3 ml/min.

© 2020 The Authors

Electrophysiology

Whole-cell current-clamp and voltage-clamp recordings were made with glass electrodes (4–6.5 MΩ) filled with a solution containing K-gluconate 120 mM, KCl 20 mM, $MgCl_2$ 2 mM, EGTA 0.6 mM, MgATP 2 mM, NaGTP 0.3 mM, HEPES 10 mM, phosphocreatine 7 mM or Cs-gluconate 100 mM, NaCl 8 mM, MgCl2 5 mM, EGTA 0.6 mM, MgATP 2 mM, NaGTP 0.3 mM, HEPES 10 mM, phosphocreatine 7 mM, QX-314 1 mM, and spermine 0.1 mM (Cs-gluconate-based solution was used to investigate I–V relationships of evoked EPSCs).

Pyramidal neurons expressing either GFP (green) or mCherry (red) were visually identified in acute slices (mPFC layers III–V) and cortical cultures using a fluorescence microscope. Electrophysiological recordings were made using a Multi Clamp 700A amplifier (Axon Instruments, Union City, CA), operating under current-clamp and voltage-clamp mode. Data were filtered at 4 kHz and acquired using pClamp 10 software (Molecular Devices, Sunnyvale, CA). All recordings were done at a holding potential −70 mV, except for SD experiments, where holding potential was −60 mV. For the I–V curve experiments, holding potential was varied from 100 to 60 mV.

The uncompensated series resistance was monitored by the delivery of −10 mV steps throughout the experiment, and only recordings with less than 15% change were analyzed.

Drugs

10 μM CNQX, 50 μM AP5, and 10 μM bicuculline methiodide (Sigma-Aldrich, Oakville, Canada) were dissolved in extracellular ACSF and applied through the perfusion system (at least 5 min before recordings). 0.5 μM TTX was always present in the ACSF if recordings were done in cultures.

Analysis of electrophysiological recordings

Synaptic events were analyzed using pClamp 10 software within at least 3 min of recordings, and individual events were detected using an automatic template search. Templates were created using the average of at least 10 events aligned by the rising of their slopes. The peak amplitude of evoked EPSCs (eEPSCs) was measured for an averaged response (five trials). Paired-pulse ratio was calculated as average for 15-20 trials. Rectification index (RI) was calculated, as a ratio of *I–V* slopes, RI = s2/s1 (Adesnik & Nicoll, 2007; Lalanne *et al*, 2016). First, we calculated slope 1 (s1) using linear regression to *AMPA currents* recorded at holding potential ≤ 0 mV, as well as an AMPAR reversal potential, E_{rev}. Next, we estimated slope 2 (s2) using a linear fit of *I–V* data recorded at positive holding potentials and constrained to intersect the *x*-axis at E_{rev}. This method allows taking into account variations of AMPA reversal potential between recordings.

Immunofluorescent staining

Mice were euthanized 3 weeks after viral delivery by a lethal dose of ketamine/xylazine and perfused with phosphate buffer saline (PBS) followed by 4% paraformaldehyde (PFA). Brains were incubated in 4% PFA 24 h at 4°C. Fixed tissue was sectioned using vibratome (Leica, VT1000S). Next, 40-μm sections were blocked and permeabilized with a permeabilization solution containing 10% normal goat serum (NGS) and 0.5% Triton X-100 (Sigma) in PBS for 2 h. Sections were incubated with primary antibodies diluted in permeabilization solution overnight at 4°C. After three washes in PBS, samples were incubated with secondary antibodies for 2 h at room temperature. After washing with PBS three times, sections were mounted using Dako mounting medium (Dako, Mississauga, Canada) and visualized with a confocal microscope (Zeiss LSM 700, Zen 2011 Software, Oberkochen, Germany).

For immunofluorescent staining of primary neurons, cells were fixed at DIV14 with 4% paraformaldehyde (PFA) and 4% sucrose mixture for 7 min at room temperature (RT). After washing three times with PBS, cells were permeabilized with 0.1% Triton X-100 in PBS for 10 min at RT. In the case of surface staining for GluA1 and GluA2, no permeabilization was performed. Cells were washed once with PBS and blocked by 10% serum in PBS for 1 h. Cells were incubated with primary antibodies in 1% serum in PBS overnight at 4°C. After washing three times with PBS, cells were incubated with secondary antibodies for 2 h at RT. Finally, coverslips were mounted using Dako mounting medium and imaged using Zeiss LSM 880. Images were processed using the Zen 2011 (Zeiss, Oberkochen, Germany). Quantifications of colocalization were performed manually using ImageJ (National Institute of Health (NIH), Bethesda, MD). For quantification of surface GluA1 and GluA2, 2–3 dendrites (ranging from 50 to 150 μm) per cell were delineated and mean signal intensity was measured using ImageJ (National Institute of Health (NIH), Bethesda, MD).

Following primary antibodies were used: mouse anti-GluA1 (1:1,000, Millipore MAB2263), mouse anti-GluA2 (1:1,000, Millipore MAB397), rabbit anti-Fxr1 (1:1,000, Abcam 129089), and mouse anti-Gsk3β (1:500, Abcam 93926).

Following secondary antibodies were used: Alexa Fluor 405, 568, or 647 (Life Technologies/Thermo Fisher Scientific, Waltham, MA, 1:1,000).

Western blot

Mice were killed by cervical dislocation, after which the heads of animals were immediately cooled by immersion in liquid nitrogen for 6 s. The medial part of the prefrontal cortex was rapidly dissected out (within 30 s) on an ice-cold surface and frozen in liquid nitrogen before protein extraction. Tissue samples were homogenized in boiling 1% SDS solution and boiled for 5 min before measurement of protein concentration. Neuro2A cells and primary cortical cultures were lysed in lysis buffer containing 50 mM Tris–HCl, 150 mM NaCl, 5 mM EDTA, protease inhibitor cocktail, 1% SDS, 0.5% Na-deoxycholate, 1% NP-40, 10 mM Na fluoride, 25 mM β-glycerophosphate, and 10 mM Na orthovanadate (Sigma-Aldrich, Oakville, Canada). Lysates were centrifuged 10,000 *g* for 30 min, and supernatants were collected. Protein concentration was measured by using a DC protein assay (Bio-Rad, Hercules, CA). Protein extracts were separated on precast 10% SDS–PAGE Tris–glycine gels (Thermo Fisher Scientific, Waltham, MA) and transferred to nitrocellulose membranes. Blots were immunostained overnight at 4°C with primary antibodies. Immune complexes were revealed using appropriate IRDye-labeled secondary antibodies from LI-COR Biotechnology (Lincoln, NE). Quantitative analyses of fluorescent IRDye signal were carried out

 © 2020 The Authors

using an Odyssey Imager and software (LI-COR Biotechnology, Lincoln, NE). For quantification, GAPDH (actin in case of Neuro2A cells) was used as a loading control for the evaluation of total protein levels. Results were further normalized to respective control conditions to allow for comparison between separate experiments. Following primary antibodies were used in the experiments: mouse anti-actin (1:10,000, Millipore, MAB1501), mouse anti-GAPDH (1:5,000, Santa Cruz, sc-322333) rabbit anti-Gsk3β (1:500, Cell Signal Technology, 9315, Danvers, MA), rabbit anti-Fxr1 (1:1,000, Abcam, 129089), rabbit ant-Fxr2 (1:500, CST #7098), rabbit anti-Fmr1 (1:500, Abcam, 17722), mouse anti-GFP (1:1,000, Rockland/VWR 600-301-215), mouse anti-GluA1 (1:1,000, Millipore, MAB2263), mouse anti-GluA2 (1:1,000, Millipore, MAB397), rabbit anti-p845GluA1 (1:1,000, Millipore, 06.773), and rabbit anti-p880GluA2 (1:1,000, Abcam, ab52180). Following secondary antibodies are used: goat anti-mouse IRDye 680 (1:10,000, Mandel 926-68020) and goat anti-rabbit IRDye 800 (1:10,000, Mandel 926-32211).

Sleep deprivation

Mice were sleep-deprived for 6 h by gentle handling starting at light onset similar to previously performed (El Helou *et al*, 2013; Freyburger *et al*, 2016). Briefly, mice were transferred to a clean cage at the beginning of SD and were gently handled by an experimenter (e.g., using a brush) every time they were showing signs of sleep (e.g., typical sleep posture, immobility). Control mice were littermates that remained undisturbed in their home cages. Sleep-deprived and control mice were killed by rapid cervical dislocation followed by brain slice recordings, HA immunoprecipitation, or Western blot experiments.

For EEG recordings, mice were kept in the same cage for the baseline condition and only transferred to a clean cage at the beginning of the fourth hour of SD. SD continued until the end of the sixth hour.

Immunoprecipitation of polyribosomes and RNA isolation

Immunoprecipitation of polyribosomes was performed as described before (Sanz *et al*, 2009). Tissue samples were lysed in homogenization buffer (50 mM Tris, pH 7.5, 100 mM KCl, 12 mM $MgCl_2$, 1% Nonidet P-40, 1 mM DTT, 100 U/ml RNase Out, 100 μg/ml cycloheximide, and Sigma protease inhibitor mixture) followed by centrifugation for 10 min at 10,000 *g*. Anti-hemagglutinin (HA) antibody (1:150; MMS-101R; BioLegend) was added into collected supernatant, and tubes were kept under constant rotation for 4 h at 4°C. Protein G magnetic beads (Life Technologies) were washed three times with homogenization buffer, then added into the mixture, and kept for constant rotation overnight at 4°C. The following day magnetic beads were washed three times with high salt buffer (50 mM Tris, pH 7.5, 300 mM KCl, 12 mM $MgCl_2$, 1% Nonidet P-40, 1 mM DTT, 100 U/ml RNase Out, 100 μg/ml cycloheximide, and Sigma protease inhibitor mixture). RNA was extracted by adding TRI reagent (Zymo research) to magnetic beads pellet followed by Direct-zol RNA Kit according to the manufacturer's instructions (Zymo Research). The RNA concentration was quantified using ND-1000 Spectrophotometer (NanoDrop Technologies).

RT–PCR qPCR

RNA was extracted from neuronal cultures using TRI reagent (Zymo Research) followed by Direct-zol RNA Kit according to the manufacturer's instructions (Zymo Research). Complementary DNA was synthesized using a reverse transcriptase SuperScript III Kit according to the manufacturer's instructions (Invitrogen). qPCR was performed using TaqMan™ Gene Expression Assays (Applied Biosystems) and TaqMan™ probes for Fxr1 (Thermo Fisher Scientific, Mm00484523_m1), Fxr2 (Thermo Fisher Scientific, Mm00839957_m1), Fmr1 (Thermo Fisher Scientific, Mm01339582_m1), and Gapdh (Thermo Fisher Scientific). Data were acquired by QuantStudio 3 Real-Time PCR System (Thermo Fisher Scientific). Relative expression analysis was performed using data from biological triplicates of each sample by QuantStudio TM Design and Analysis Software (Thermo Fisher Scientific).

RNAseq analysis

Quality control

The quality control metrics for the RNAseq data were obtained using the tool RNA-SeQC (v1.1.7). For more information, visit their website found here: http://www.broadinstitute.org/cancer/cga/rna-seqc. This program takes aligned files as input and delivers a series of plots and statistics for each sample. Based on the output for each sample, the RNA sequencing quality was deemed acceptable for further analysis.

Processing pipeline

All raw FASTQ files were aligned to the appropriate mouse genome (GRCm38) using the HISAT2 aligner. HISAT2 is a fast and sensitive alignment program that uses a large set of small graph FM (GFM) indexes that collectively cover the whole reference genome. These local indexes, in conjunction with a series of alignment strategies, ensure a rapid and accurate alignment of sequencing reads. Accessory programs for the alignment stage include SAMTOOLS (v1.3.1) and BEDTOOLS (v2.26.0). Alignment files were sorted by their genomic location and indexed using SAMTOOLS. These sorted binary SAM (BAM) files were then used as input for StringTie (v1.3.4), which assembles RNAseq alignments into potential transcripts. It uses a novel network flow algorithm as well as an optional *de novo* assembly step to assemble and quantitate full-length transcripts representing multiple splice variants for each gene locus. Finally, in order to identify differentially expressed genes between samples, the Ballgown R-package was implemented (v3.4.3). Transcript-level FPKMs were estimated using TableMaker. Expression was estimated for each transcript, exon, and intron (junction) in the assembly. All of the statistical analysis (organization, visualization, etc.) was conducted with the tools available within the Ballgown package.

Differential expression analysis

The statistical test applied to these data was a parametric *F*-test comparing nested linear models; details are available in the Ballgown manuscript. Briefly, two models are fit to each feature, using the expression as the outcome: one including the covariate of interest (e.g., case/control status) and one not including that covariate. An *F* statistic and *P*-value are calculated using the fits of the two

© 2020 The Authors

models. A significant *P*-value means that the model including the covariate of interest fits significantly better than the model without that covariate, indicating differential expression. All the differentially expressed transcripts (DETs) with $P < 0.05$ were selected for further analysis. Differential expression testing was carried out for the following comparisons: Ctrl/S vs. Ctrl/SD and Ctrl/SD vs. Fxr1 overexpression/SD.

Gene set enrichment analysis

First DETs were filtered. All selected transcripts had a mean expression > 0.5 FKPM. Fold change (FC) threshold was set to $0.7 < FC > 1.3$. Enrichment analyses and visualization were performed following the pipeline described in Reimand *et al* (2019). Enrichment analysis was performed using gProfiler (https://biit.cs.ut.ee/gprofiler/gost). Term size for pathways was selected to be min 5 and max 150. Only pathways passing significance threshold of 0.05 were selected. Gene enrichment in Gene Ontology Biological pathways (GO:BP) was selected. Then, .GEM and .GMT files were downloaded from gProfiler and were used in EnrichmentMap app of Cytoscape (Ver 3.7.1) for visualization. Following parameters of EnrichmentMap were used: FDR *q* value cutoff < 0.05, Jaccard combined > 0.375, overlap > 0.5, and Prefuse Force Directed layout were chosen. Then, ClusterMaker2 App was used to cluster enriched pathways based on similarity, and AutoAnnotate and WordCloud Apps were used to name clusters of enriched pathways using default parameters. The final pictures of the clusters of enriched pathways (in case of Ctrl/S vs. Ctrl/SD comparison, only top 10 biggest clusters are shown) are shown in Fig 7. The list of all the enriched pathways is shown in Tables EV4 and EV5.

Enrichment in SynGO localization and function was performed using default parameters (https://syngoportal.org/) against brain expressed background. Significant enrichment was considered at 5% FDR (FDR < 0.05). The graphical representation is shown in Fig 7, and the whole list of pathways and genes is shown in Tables EV6 and EV7.

Quantification and statistical analysis

The data are presented as means ± SEM. For comparison between two groups, two-tailed *t*-test was used. For comparison between multiple groups, one-way ANOVA was used followed by the Bonferroni-corrected pairwise comparisons using GraphPad Prism 5 software (La Jolla, CA) (*$P < 0.05$, **$P < 0.01$, ***$P < 0.001$).

Data availability

RNAseq data and analysis are deposited to GEO (GSE139576; http://www.ncbi.nlm.nih.gov/geo/query/acc.cgi?acc=GSE139576). Viral vectors are or will be made available through Addgene. For additional materials, contact the lead author.

Expanded View for this article is available online.

Acknowledgements
The authors acknowledge Chloé Provost and Julien Dufort-Gervais for technical help with AAV injection/EEG implantation surgery. JMB is Canada Research Chair in Molecular Psychiatry. VM is Canada Research Chair in Sleep Molecular Physiology. This work was supported by grants from Canada Institutes of Health Research (CIHR, PJT-148568) to JMB, and salary awards from CIHR and Fonds de recherche du Québec—Santé (FRQS) to VM. JMB is NARSAD independent investigator and One-Mind Rising Star awardee.

Author contributions
J-MB conceived the study. J-MB and JK designed the experiments. J-MB, JK, AE, and VM wrote the manuscript. JK performed design and testing of CRISPR/Cas9 *in vitro* and *in vivo*, stereotaxic injections, protein expression analysis *in vitro* and *in vivo*, primary neuronal culture preparation, drug treatment, and receptor surface staining and quantification, SD, RiboTag IP, and RNA extraction and RNAseq data analysis. DC performed additional primary culture and biochemical analysis. AE and SC performed whole-cell patch-clamp recordings and data analysis. AM performed CRISPR/Cas9 KO experiments with puromycin selection followed by detection of Fxr1 expression. LB performed cloning and luciferase assay. VM performed EEG recordings and analyses. VM, AM, and TSS participated in mouse SD experiments. JMB, VM, and KT provided technical, financial, and intellectual support.

Conflict of interest
The authors declare that they have no conflict of interest.

References

Adesnik H, Nicoll RA (2007) Conservation of glutamate receptor 2-containing AMPA receptors during long-term potentiation. *J Neurosci* 27: 4598 – 4602

Areal CC, Warby SC, Mongrain V (2017) Sleep loss and structural plasticity. *Curr Opin Neurobiol* 44: 1 – 7

Arrubla J, Farrher E, Strippelmann J, Tse DHY, Grinberg F, Shah NJ, Neuner I (2017) Microstructural and functional correlates of glutamate concentration in the posterior cingulate cortex. *J Neurosci Res* 95: 1796 – 1808

Ascano M, Mukherjee N, Bandaru P, Miller JB, Nusbaum JD, Corcoran DL, Langlois C, Munschauer M, Dewell S, Hafner M *et al* (2012) FMRP targets distinct mRNA sequence elements to regulate protein expression. *Nature* 492: 382 – 386

Beaulieu JM, Gainetdinov RR, Caron MG (2009) Akt/GSK3 signaling in the action of psychotropic drugs. *Annu Rev Pharmacol Toxicol* 49: 327 – 347

Beique JC, Na Y, Kuhl D, Worley PF, Huganir RL (2011) Arc-dependent synapse-specific homeostatic plasticity. *Proc Natl Acad Sci USA* 108: 816 – 821

Billiard M (1987) Lithium carbonate: effects on sleep patterns of normal and depressed subjects and its use in sleep-wake pathology. *Pharmacopsychiatry* 20: 195 – 196

Brodl E, Winkler A, Macheroux P (2018) Molecular mechanisms of bacterial bioluminescence. *Comput Struct Biotechnol J* 16: 551 – 564

Broussard JI, Givens B (2010) Low frequency oscillations in rat posterior parietal cortex are differentially activated by cues and distractors. *Neurobiol Learn Mem* 94: 191 – 198

Cheung J, Ruoff C, Moore H, Hagerman KA, Perez J, Sakamuri S, Warby SC, Mignot E, Day J, Sampson J (2018) Increased EEG theta spectral power in sleep in myotonic dystrophy type 1. *J Clin Sleep Med* 14: 229 – 235

Cong L, Ran FA, Cox D, Lin S, Barretto R, Habib N, Hsu PD, Wu X, Jiang W, Marraffini LA *et al* (2013) Multiplex genome engineering using CRISPR/Cas systems. *Science* 339: 819 – 823

 © 2020 The Authors

Cook D, Sanchez-Carbente MeR, Lachance C, Radzioch D, Tremblay S, Khandjian EW, DesGroseillers L, Murai KK (2011) Fragile X related protein 1 clusters with ribosomes and messenger RNAs at a subset of dendritic spines in the mouse hippocampus. *PLoS ONE* 6: e26120

Cook D, Nuro E, Jones EV, Altimimi HF, Farmer WT, Gandin V, Hanna E, Zong R, Barbon A, Nelson DL *et al* (2014) FXR1P limits long-term memory, long-lasting synaptic potentiation, and *de novo* GluA2 translation. *Cell Rep* 9: 1402 – 1416

Curie T, Mongrain V, Dorsaz S, Mang GM, Emmenegger Y, Franken P (2013) Homeostatic and circadian contribution to EEG and molecular state variables of sleep regulation. *Sleep* 36: 311 – 323

Dashti HS, Jones SE, Wood AR, Lane JM, van Hees VT, Wang H, Rhodes JA, Song Y, Patel K, Anderson SG *et al* (2019) Genome-wide association study identifies genetic loci for self-reported habitual sleep duration supported by accelerometer-derived estimates. *Nat Commun* 10: 1100

Del'Guidice T, Latapy C, Rampino A, Khlghatyan J, Lemasson M, Gelao B, Quarto T, Rizzo G, Barbeau A, Lamarre C *et al* (2015) FXR1P is a GSK3β substrate regulating mood and emotion processing. *Proc Natl Acad Sci USA* 112: E4610 – E4619

van Diepen RM, Miller LM, Mazaheri A, Geng JJ (2016) The role of alpha activity in spatial and feature-based attention. *eNeuro* 3: ENEURO.0204-16.2016

Diering GH, Gustina AS, Huganir RL (2014) PKA-GluA1 coupling via AKAP5 controls AMPA receptor phosphorylation and cell-surface targeting during bidirectional homeostatic plasticity. *Neuron* 84: 790 – 805

Diering GH, Nirujogi RS, Roth RH, Worley PF, Pandey A, Huganir RL (2017) Homer1a drives homeostatic scaling-down of excitatory synapses during sleep. *Science* 355: 511 – 515

El Fatimy R, Davidovic L, Tremblay S, Jaglin X, Dury A, Robert C, De Koninck P, Khandjian EW (2016) Tracking the fragile X mental retardation protein in a highly ordered neuronal RiboNucleoParticles population: a link between stalled polyribosomes and RNA granules. *PLoS Genet* 12: e1006192

El Helou J, Belanger-Nelson E, Freyburger M, Dorsaz S, Curie T, La Spada F, Gaudreault PO, Beaumont E, Pouliot P, Lesage F *et al* (2013) Neuroligin-1 links neuronal activity to sleep-wake regulation. *Proc Natl Acad Sci USA* 110: 9974 – 9979

Freland L, Beaulieu JM (2012) Inhibition of GSK3 by lithium, from single molecules to signaling networks. *Front Mol Neurosci* 5: 14

Freyburger M, Pierre A, Paquette G, Belanger-Nelson E, Bedont J, Gaudreault PO, Drolet G, Laforest S, Blackshaw S, Cermakian N *et al* (2016) EphA4 is involved in sleep regulation but not in the electrophysiological response to sleep deprivation. *Sleep* 39: 613 – 624

Fu AK, Ip NY (2017) Regulation of postsynaptic signaling in structural synaptic plasticity. *Curr Opin Neurobiol* 45: 148 – 155

Gao R, Penzes P (2015) Common mechanisms of excitatory and inhibitory imbalance in schizophrenia and autism spectrum disorders. *Curr Mol Med* 15: 146 – 167

Gideons ES, Lin PY, Mahgoub M, Kavalali ET, Monteggia LM (2017) Chronic lithium treatment elicits its antimanic effects via BDNF-TrkB dependent synaptic downscaling. *Elife* 6: e25480

Guo W, Polich ED, Su J, Gao Y, Christopher DM, Allan AM, Wang M, Wang F, Wang G, Zhao X (2015) Fragile X proteins FMRP and FXR2P control synaptic GluA1 expression and neuronal maturation via distinct mechanisms. *Cell Rep* 11: 1651 – 1666

Hengen KB, Torrado Pacheco A, McGregor JN, Van Hooser SD, Turrigiano GG (2016) Neuronal firing rate homeostasis is inhibited by sleep and promoted by wake. *Cell* 165: 180 – 191

Infarinato F, Rahman A, Del Percio C, Lamberty Y, Bordet R, Richardson JC, Forloni G, Drinkenburg W, Lopez S, Aujard F *et al* (2015) On-going frontal alpha rhythms are dominant in passive state and desynchronize in active state in adult gray mouse lemurs. *PLoS ONE* 10: e0143719

Jansen PR, Watanabe K, Stringer S, Skene N, Bryois J, Hammerschlag AR, de Leeuw CA, Benjamins JS, Muñoz-Manchado AB, Nagel M *et al* (2019) Genome-wide analysis of insomnia in 1,331,010 individuals identifies new risk loci and functional pathways. *Nat Genet* 51: 394 – 403

Kavalali ET, Monteggia LM (2020) Targeting homeostatic synaptic plasticity for treatment of mood disorders. *Neuron* 106: 715 – 726

Khlghatyan J, Beaulieu JM (2018) Are FXR family proteins integrators of dopamine signaling and glutamatergic neurotransmission in mental illnesses? *Front Synaptic Neurosci* 10: 22

Khlghatyan J, Evstratova A, Chamberland S, Marakhovskaia A, Bahremand A, Toth K, Beaulieu JM (2018) Mental Illnesses-associated Fxr1 and its negative regulator Gsk3β are modulators of anxiety and glutamatergic neurotransmission. *Front Mol Neurosci* 11: 119

Koopmans F, van Nierop P, Andres-Alonso M, Byrnes A, Cijsouw T, Coba MP, Cornelisse LN, Farrell RJ, Goldschmidt HL, Howrigan DP *et al* (2019) SynGO: an evidence-based, expert-curated knowledge base for the synapse. *Neuron* 103: 217 – 234

Kronman H, Richter F, Labonté B, Chandra R, Zhao S, Hoffman G, Lobo MK, Schadt EE, Nestler EJ (2019) Biology and bias in cell type-specific RNAseq of nucleus accumbens medium spiny neurons. *Sci Rep* 9: 8350

Lalanne T, Oyrer J, Mancino A, Gregor E, Chung A, Huynh L, Burwell S, Maheux J, Farrant M, Sjostrom PJ (2016) Synapse-specific expression of calcium-permeable AMPA receptors in neocortical layer 5. *J Physiol* 594: 837 – 861

Lee KY, Jewett KA, Chung HJ, Tsai NP (2018) Loss of fragile X protein FMRP impairs homeostatic synaptic downscaling through tumor suppressor p53 and ubiquitin E3 ligase Nedd4-2. *Hum Mol Genet* 27: 2805 – 2816

Liu ZW, Faraguna U, Cirelli C, Tononi G, Gao XB (2010) Direct evidence for wake-related increases and sleep-related decreases in synaptic strength in rodent cortex. *J Neurosci* 30: 8671 – 8675

Liu X, Kelsoe JR, Greenwood TA, Bipolar Genome Study (BiGS) (2016) A genome-wide association study of bipolar disorder with comorbid eating disorder replicates the SOX2-OT region. *J Affect Disord* 189: 141 – 149

Mang GM, Franken P (2015) Genetic dissection of sleep homeostasis. *Curr Top Behav Neurosci* 25: 25 – 63

McEwen BS (2012) Brain on stress: how the social environment gets under the skin. *Proc Natl Acad Sci USA* 109(Suppl 2): 17180 – 17185

McEwen BS, Karatsoreos IN (2015) Sleep deprivation and circadian disruption: stress, allostasis, and allostatic load. *Sleep Med Clin* 10: 1 – 10

McGinley MJ, Vinck M, Reimer J, Batista-Brito R, Zagha E, Cadwell CR, Tolias AS, Cardin JA, McCormick DA (2015) Waking state: rapid variations modulate neural and behavioral responses. *Neuron* 87: 1143 – 1161

Nelson SB, Valakh V (2015) Excitatory/inhibitory balance and circuit homeostasis in autism spectrum disorders. *Neuron* 87: 684 – 698

Picchioni D, Reith RM, Nadel JL, Smith CB (2014) Sleep, plasticity and the pathophysiology of neurodevelopmental disorders: the potential roles of protein synthesis and other cellular processes. *Brain Sci* 4: 150 – 201

Qie S, Majumder M, Mackiewicz K, Howley BV, Peterson YK, Howe PH, Palanisamy V, Diehl JA (2017) Fbxo4-mediated degradation of Fxr1 suppresses tumorigenesis in head and neck squamous cell carcinoma. *Nat Commun* 8: 1534

Ran FA, Hsu PD, Wright J, Agarwala V, Scott DA, Zhang F (2013) Genome engineering using the CRISPR-Cas9 system. *Nat Protoc* 8: 2281 – 2308

© 2020 The Authors

Raven F, Van der Zee EA, Meerlo P, Havekes R (2018) The role of sleep in regulating structural plasticity and synaptic strength: implications for memory and cognitive function. *Sleep Med Rev* 39: 3 – 11

Reimand J, Isserlin R, Voisin V, Kucera M, Tannus-Lopes C, Rostamianfar A, Wadi L, Meyer M, Wong J, Xu C *et al* (2019) Pathway enrichment analysis and visualization of omics data using g:Profiler, GSEA, Cytoscape and EnrichmentMap. *Nat Protoc* 14: 482 – 517

Ripke S, Neale BM, Corvin A, Walters JTR, Farh K-H, Holmans PA, Lee P, Bulik-Sullivan B, Collier DA, Huang H *et al* (2014) Biological insights from 108 schizophreniaassociated genetic loci. *Nature* 511: 421 – 427

Salmela E, Renvall H, Kujala J, Hakosalo O, Illman M, Vihla M, Leinonen E, Salmelin R, Kere J (2016) Evidence for genetic regulation of the human parieto-occipital 10-Hz rhythmic activity. *Eur J Neurosci* 44: 1963 – 1971

Sanz E, Yang L, Su T, Morris DR, McKnight GS, Amieux PS (2009) Cell-type-specific isolation of ribosome-associated mRNA from complex tissues. *Proc Natl Acad Sci USA* 106: 13939 – 13944

Schanzenbacher CT, Sambandan S, Langer JD, Schuman EM (2016) Nascent proteome remodeling following homeostatic scaling at hippocampal synapses. *Neuron* 92: 358 – 371

Seok BS, Cao F, Bélanger-Nelson E, Provost C, Gibbs S, Jia Z, Mongrain V (2018) The effect of Neuroligin-2 absence on sleep architecture and electroencephalographic activity in mice. *Mol Brain* 11: 52

Soden ME, Chen L (2010) Fragile X protein FMRP is required for homeostatic plasticity and regulation of synaptic strength by retinoic acid. *J Neurosci* 30: 16910 – 16921

Swift JL, Godin AG, Dore K, Freland L, Bouchard N, Nimmo C, Sergeev M, De Koninck Y, Wiseman PW, Beaulieu JM (2011) Quantification of receptor tyrosine kinase transactivation through direct dimerization and surface density measurements in single cells. *Proc Natl Acad Sci U S A* 108: 7016 – 7021

Tatavarty V, Torrado Pacheco A, Groves Kuhnle C, Lin H, Koundinya P, Miska NJ, Hengen KB, Wagner FF, Van Hooser SD, Turrigiano GG (2020) Autism-associated Shank3 is essential for homeostatic compensation in rodent V1. *Neuron* 106: 769 – 777

Tononi G, Cirelli C (2014) Sleep and the price of plasticity: from synaptic and cellular homeostasis to memory consolidation and integration. *Neuron* 81: 12 – 34

Turrigiano GG, Leslie KR, Desai NS, Rutherford LC, Nelson SB (1998) Activity-dependent scaling of quantal amplitude in neocortical neurons. *Nature* 391: 892 – 896

Turrigiano GG (2008) The self-tuning neuron: synaptic scaling of excitatory synapses. *Cell* 135: 422 – 435

Turrigiano G (2012) Homeostatic synaptic plasticity: local and global mechanisms for stabilizing neuronal function. *Cold Spring Harb Perspect Biol* 4: a005736

Vassalli A, Franken P (2017) Hypocretin (orexin) is critical in sustaining theta/gamma-rich waking behaviors that drive sleep need. *Proc Natl Acad Sci USA* 114: E5464 – E5473

Vico Varela E, Etter G, Williams S (2019) Excitatory-inhibitory imbalance in Alzheimer's disease and therapeutic significance. *Neurobiol Dis* 127: 605 – 615

Vijayan S, Kopell NJ (2012) Thalamic model of awake alpha oscillations and implications for stimulus processing. *Proc Natl Acad Sci USA* 109: 18553 – 18558

Vitureira N, Letellier M, Goda Y (2012) Homeostatic synaptic plasticity: from single synapses to neural circuits. *Curr Opin Neurobiol* 22: 516 – 521

de Vivo L, Bellesi M, Marshall W, Bushong EA, Ellisman MH, Tononi G, Cirelli C (2017) Ultrastructural evidence for synaptic scaling across the wake/sleep cycle. *Science* 355: 507 – 510

Vyazovskiy VV, Cirelli C, Pfister-Genskow M, Faraguna U, Tononi G (2008) Molecular and electrophysiological evidence for net synaptic potentiation in wake and depression in sleep. *Nat Neurosci* 11: 200 – 208

Whitman SA, Cover C, Yu L, Nelson DL, Zarnescu DC, Gregorio CC (2011) Desmoplakin and talin2 are novel mRNA targets of fragile X-related protein-1 in cardiac muscle. *Circ Res* 109: 262 – 271

Wondolowski J, Dickman D (2013) Emerging links between homeostatic synaptic plasticity and neurological disease. *Front Cell Neurosci* 7: 223

Woolfrey KM, Srivastava DP (2016) Control of dendritic spine morphological and functional plasticity by small GTPases. *Neural Plast* 2016: 3025948

License: This is an open access article under the terms of the Creative Commons Attribution-NonCommercial-NoDerivs 4.0 License, which permits use and distribution in any medium, provided the original work is properly cited, the use is non-commercial and no modifications or adaptations are made.